HAL
archives-ouvertes.fr

Validation of traffic flow models on processed GPS data

Alessandra Cabassi, Paola Goatin

▶ **To cite this version:**

Alessandra Cabassi, Paola Goatin. Validation of traffic flow models on processed GPS data. [Research Report] RR-8382, INRIA. 2013, pp.43. <hal-00876311>

HAL Id: hal-00876311
https://hal.inria.fr/hal-00876311

Submitted on 24 Oct 2013

HAL is a multi-disciplinary open access archive for the deposit and dissemination of scientific research documents, whether they are published or not. The documents may come from teaching and research institutions in France or abroad, or from public or private research centers.

L'archive ouverte pluridisciplinaire **HAL**, est destinée au dépôt et à la diffusion de documents scientifiques de niveau recherche, publiés ou non, émanant des établissements d'enseignement et de recherche français ou étrangers, des laboratoires publics ou privés.

Validation of traffic flow models on processed GPS data

Alessandra Cabassi, Paola Goatin

RESEARCH REPORT

N° 8382

September 2013

Project-Team OPALE

ISSN 0249-6399 ISRN INRIA/RR--8382--FR+ENG

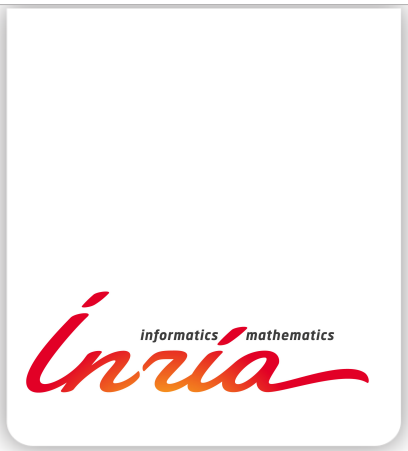

Validation of traffic flow models on processed GPS data

Alessandra Cabassi, Paola Goatin *

Project-Team OPALE

Research Report n° 8382 — September 2013 — 40 pages

Abstract: Macroscopic traffic flow models allow describing the spatio-temporal evolution of traffic density. Their sound mathematical structure consisting of partial differential equations of hyperbolic type and the related efficient numerical schemes enable fast computations to monitor traffic evolution. The aim of the internship was to validate these models against processed data provided by the industrial partners Autoroutes Trafic and VINCI Autoroutes. Targeted applications included congestion detection, congestion starting and ending points location, congestion evolution in time and travelling time estimation. To this end, we used the first-order Lighthill–Whitham–Richards model with a parabolic-linear flux function. The first part of the internship has been devoted to parameters identification, performing different calibration methods and finally choosing a hybrid compromise in order to exploit to the best the available data. Afterwards, numerical simulations have been performed on a selected case study, and results have been compared to real data to assess the validity and relevancy of the model. Numerical simulations consisted in established finite volume discretization of the hyperbolic partial differential equation. Numerical results show that, while reproducing traffic evolution during all the morning is really challenging, short term predictions are reliable.

Key-words: Traffic flow models, hyperbolic PDE, model calibration

* INRIA Sophia Antipolis Méditerranée, OPALE Project-Team

RESEARCH CENTRE
SOPHIA ANTIPOLIS – MÉDITERRANÉE

2004 route des Lucioles - BP 93
06902 Sophia Antipolis Cedex

Validation de modèles de trafic routier avec des données GPS

Résumé : Les modèles macroscopiques de trafic permettent de décrire l'évolution spatio-temporelle de la densité du trafic. Leur structure mathématique constituée par des équations aux dérivées partielles de type hyperbolique rend possible leur implémentation avec des schémas numériques efficaces, permettant ainsi d'effectuer des calculs rapides pour suivre l'évolution du trafic. L'objectif du stage était de valider ces modèles avec des données expérimentales fournies par les sociétés Autoroutes Trafic et VINCI Autoroutes. Les applications visées incluent la détection des embouteillages, la localisation de leurs points de début et de fin, leur évolution dans le temps et l'estimation des temps de parcours. Pour cela, nous avons utilisé le modèle du premier ordre de Lighthill-Whitham-Richards avec une fonction flux parabolique-linéaire. La première partie du stage a été consacrée à l'identification des paramètres. Pendant cette phase, plusieurs méthodes de calibration du modèle ont été testées, dans le but d'exploiter au mieux les données que nous avions à disposition. Ensuite, des simulations numériques ont été réalisées sur des cas d'études et les résultats ont été comparés aux données réelles afin d'évaluer la validité et la pertinence du modèle. Les simulations numériques ont été faites parmi une méthode de discrétisation aux volumes finis de l'équation aux dérivées partielles hyperbolique. Les résultats numériques montrent que, grâce à ce modèle, des prévisions à court terme peuvent être facilement effectuées, tandis que la reproduction de l'évolution du trafic pendant toute la matinée reste un véritable défi.

Mots-clés : Modèles macroscopiques de trafic, EDP hyperbolique, calibration du modèle

Contents

1 Introduction

Mathematical models for vehicular traffic have been investigated since long time. The traffic simulation problem is challenging due to the rapid changes as well as random events which can happen. It was attacked by means of macro-, meso-, and microscopic models, and a huge bulk of literature is now available, see for example [Piccoli Garavello 2006].

In this essay we restrict ourselves to macroscopic models, i.e. models where the flow of cars along a road is assimilated to the flow of fluid particles, for which suitable balance or conservation laws can be written. For this reason, macroscopic models are often called in the present context *fluid dynamic* or *hydrodynamic* models. This kind of models are particularly suitable to deal with large data sets, as it is our case, and are able to describe collective phenomena such as the evolution of congested regions or the propagation velocity of traffic waves. Whereas many experiments using real data have been done using loop sensors' data, only a few very recent works have used mobile sensors data, coming from GPS units installed on mobile phones of the drivers (see [Herrera Work et al. 2009] and [Cristiani de Fabritiis Piccoli 2010]). The predictions are processed such that they can be distributed via traffic message channel, variable-message signs, or serve as input for connected navigation devices.

Concerning this project, even if both types of data were available, the model we've conceived exclusively needs GPS data. Loop detectors' data have been used to validate and adjust the model. The study aims at applying macroscopic traffic flow models to improve the process of specific situations detection or prediction, with the global aim to contribute to sustainable traffic management.

In particular, the portion of the A8 highway (also known as *La Provençale*) that runs between Antibes and Nice has been studied. This section of highway is 17,5 km long and was selected specifically for its complex traffic properties: in particular, the narrowing of the street in a highly frequented area causes frequent congestions. The road is divided in several segments, and the algorithm is executed in each segment separately (sharing information at the boundaries). In this way it is possible to choose different model parameters in each segment, thus optimizing the algorithm.

The essay is organized as follows. In chapters 2 and 3 we introduce a mathematical model of traffic evolution and its numerical approximation. The first part of chapter 4 is dedicated to the highway's characteristics, while in the second one we present data at our disposal and explain how they have been processed. In chapter 5 different methods of calibrating parameters are listed, together with the results they lead to in our case. In chapter 6 we present the numerical results. Finally some conclusions end the essay.

2 Mathematical model

Macroscopic traffic models describe the evolution of vehicle positions in term of macroscopic variables as the density and the average speed of cars. An unidirectional road is modelled by an interval $I = [a, b]$ of $\mathbb{R}$ $(a < b)$ and the density $\rho(t, x)$ and the average velocity $v(t, x)$ depend on the time t and on $x \in I$. The simplest model is the scalar one proposed independently by Lighthill and Whitham in 1955 and by Richards in 1956. It is based on the conservation of cars and is described by a single equation in conservation form.

The main objective of this chapter is to describe this mathematical model of traffic evolution, which expresses conservation of vehicles, known as the Lighthill-Whitham-Richards (LWR) partial differential equation (PDE), and review its important mathematical attributes.

The chapter is organized as follows. In Section 2.1 we recall the derivation of the LWR PDE as an integral equation expressing conservation of vehicles on a stretch of roadway, and note that when the density is smooth, it yields the well-known LWR PDE. Section 2.2 is dedicated to the presentation of some typical flux functions for traffic models, and the following one presents the solution of the Riemann problem for those models.

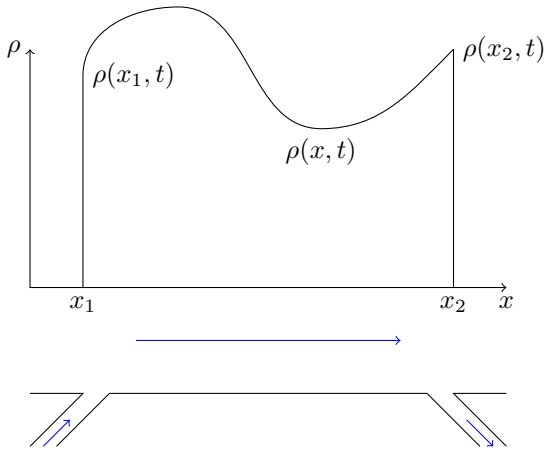

Figure 1: Conservation of vehicle density on a highway stretch

2.1 Mass conservation law for traffic

Let $\rho(x,t)$ be the vehicle density (the number of vehicles per unit length) at the point x in space and t in time, and let f be the flux (number of vehicles per unit time) as a function of the density. The flux function f is defined in an interval $[0,\rho_{max}]$, where ρ_{max} is the maximal density, sometimes referred to as *jam density*. The total number of vehicles on a segment between two points x_1 and x_2 is given by $\int_{x_1}^{x_2}\rho(x,t)\,\mathrm{d}x$. Assuming vehicles do not appear or disappear within the segment, we have:

$$\frac{\mathrm{d}}{\mathrm{d}t}\int_{x_1}^{x_2}\rho(x,t)\,\mathrm{d}x = f(\rho(x_1,t)) - f(\rho(x_2,t)) = \tag{1}$$

$$= -f(\rho(x,t))|_{x_1}^{x_2} = \int_{x_1}^{x_2}\frac{\partial}{\partial x}f(\rho(x,t))\,\mathrm{d}x$$

Equation (1) can be understood in the following way. Consider a segment of roadway shown in Figure 1, with vehicles entering from the left and exiting to the right. The change in the number of vehicles in the segment over time is just the difference between the number vehicles which entered at x_1, given by $f(\rho(x_1,t))$ and the number that leave at x_2, given by $f(\rho(x_2,t))$.

When $\rho(x,t)$ is smooth, 1 can be rewritten as

$$\int_{x_1}^{x_2}\left(\frac{\partial\rho(x,t)}{\partial t}+\frac{\partial f(\rho(x,t))}{\partial x}\right)\mathrm{d}x = 0 \tag{2}$$

Since (2) holds for any x_1 and x_2, we obtain the seminal LWR PDE model

$$\frac{\partial\rho(x,t)}{\partial t}+\frac{\partial f(\rho(x,t))}{\partial x} = 0 \quad (x,t)\in(-\infty,+\infty)\times[0,+\infty) \tag{3}$$

$$\rho(x,0) = \rho_0(x) \quad x\in(-\infty,+\infty) \tag{4}$$

which is the macroscopic traffic flow model expressing conservation of vehicles along and infinite stretch of roadway from time $t=0$ through $t=T$, augmented with the initial condition ρ_0. In

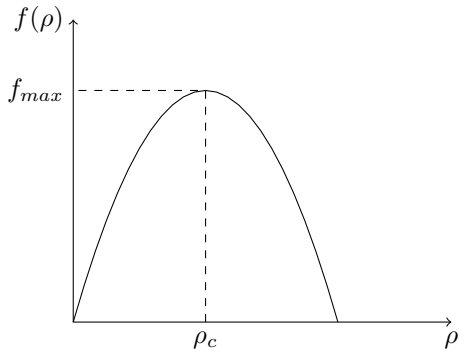

Figure 2: Greenshield's fundamental diagram

this case, the average speed v is assumed to be a function depending only on the density, and the flux is given by ρv. For simplicity we suppose that

1. f is a C^2 function;
2. f is a strictly concave function;
3. $f(0) = f(\rho_{max}) = 0$.

2.2 Fundamental diagrams

The main assumption for the Lighthill-Whitham Richards model is that the average velocity v depends only on the density of the cars. A reasonable property of v is that it is a decreasing function of the density. The law giving the flux as function of the density is called *fundamental diagram*.

Extensive studies of the empirical correlation between flow rate and density have been performed in the traffic flow literature. We describe here various fundamental diagrams assigning the velocity function $v = v(\rho)$, thus the flux is simply obtained multiplying by the density ρ.

Greenshield's fundamental diagram The simplest fundamental diagram is obtained setting v to be a linear function of the density i.e.

$$v_G(\rho) = v_{max}\left(1 - \frac{\rho}{\rho_{max}}\right), \tag{5}$$

(cf. Fig. 2) where v_{max} is the *free speed* or *desired speed* and corresponds to the minimum of the actual desired speed of the drivers, the physically possible attainable speed and, possibly, an administrated speed limit.

Daganzo-Newell's fundamental diagram The widely used Daganzo-Newell velocity function assumes a constant velocity in free-flow and a hyperbolic velocity in congestion (cf. Fig. 3)

$$v_{DN}(\rho) = \begin{cases} v_{max} & \text{if } \rho \le \rho_c \\ -\omega_f\left(1 - \frac{\rho_{max}}{\rho}\right) & \text{otherwise} \end{cases}. \tag{6}$$

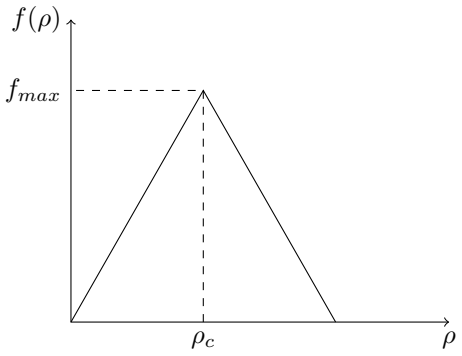

Figure 3: Daganzo-Newell's fundamental diagram

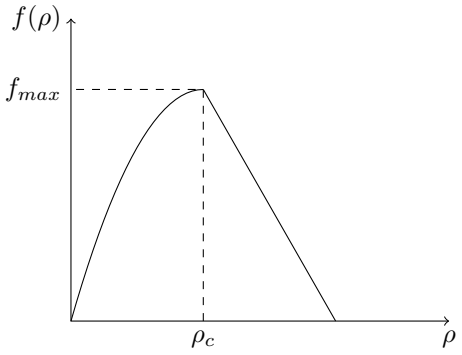

Figure 4: Quadratic-linear fundamental diagram

Here ρ_c represents the critical density (the limit density between the fluid and congested phases) and ω_f is the backwards propagating wave-speed.

Daganzo-Newell's modified fundamental diagram Because the Daganzo-Newell velocity function is not strictly monotonic in free-flow, it cannot be inverted. In order to use the Daganzo-Newell model in situations where invertible velocity functions are needed, it has been approximated in [Work et al. 2010] by velocity function with a linear expression in free-flow and a hyperbolic expression in congestion

$$v_{HL} = \begin{cases} v_{max}\left(1 - \frac{\rho}{\rho_{max}}\right) & \text{if } \rho \leq \rho_c \\ -\omega_f\left(1 - \frac{\rho_{max}}{\rho}\right) & \text{otherwise} \end{cases}, \tag{7}$$

see Fig. 4. For continuity of the flux at the critical density ρ_c, the additional relation

$$\frac{\rho_c}{\rho_{max}} = \frac{\omega_f}{v_{max}} \tag{8}$$

must be satisfied.

Moreover, looking at our GPS data, we found that the two ρ_{max} in the first and second line cases are not necessarily equal. So we called the first one ρ_a and let the second one be ρ_{max},

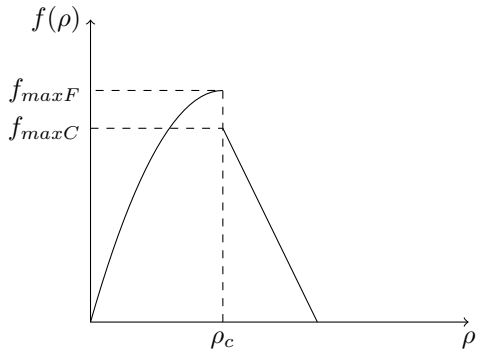

Figure 5: Quadratic-linear fundamental diagram with capacity drop

as it is the value that will actually represent the maximal number of cars that can stay in one kilometer of road. The continuity condition must be changed accordingly.

$$v_{HL} = \begin{cases} v_{max}\left(1 - \frac{\rho}{\rho_a}\right) & \text{if } \rho \leq \rho_c \\ -\omega_f\left(1 - \frac{\rho_{max}}{\rho}\right) & \text{otherwise} \end{cases} . \tag{9}$$

2.2.1 Capacity drop

A striking feature of many experimental results is the presence of an apparent discontinuity that separates the free flow (low density) and congested (high density) states. This phenomenon is also referred to as *capacity drop*. In this case traffic shows hysteresis effects, i.e. the dynamics does not only depend on the traffic demand but also on the history of the system. According to this theory, the velocity function is defined as

$$v_{CD} = \begin{cases} v_f(\rho) & \text{if } 0 \leq \rho < \rho_c \\ v_c(\rho) & \text{if } \rho_c \leq \rho \leq \rho_{max} \end{cases} , \tag{10}$$

where it holds $v_f(\rho_c) > v_c(\rho_c)$. The resulting discontinuous velocity function for the HL model is shown in Fig. 5. When the traffic breaks down, the system state switches from the *free branch* v_f onto the *congested branch* v_c, lowering the maximum possible flow. This implies that once a traffic jam has emerged, the traffic demand has to fall to a much lower value to dissolve the jam. The flow-density diagram describing this phenomenon is also said to have an *inverse-λ form*.

2.3 Riemann problems

Assumptions 1 and 2 in Section 2.1 imply that equation (3) is strictly hyperbolic and the characteristic field is genuinely nonlinear. Consider the Riemann problem for (3) with initial datum

$$\rho(0,x) = \begin{cases} \rho^- & \text{if } x < 0 \\ \rho^+ & \text{if } x > 0. \end{cases} \tag{11}$$

If $\rho^- < \rho^+$, then 1 and 2 imply that $f'(\rho^-) > f'(\rho^+)$ and so the entropy-admissible solution is given by the shock wave

$$\rho(x,t) = \begin{cases} \rho^- & \text{if } x < \lambda t \\ \rho^+ & \text{if } x > \lambda t \end{cases} \tag{12}$$

where, by the Rankine-Hugoniot condition

$$\lambda = \frac{f(\rho^+) - f(\rho^-)}{\rho^+ - \rho^-}. \tag{13}$$

The speed of the wave is positive if $f(\rho^+) > f(\rho^-)$, while is negative if $f(\rho^+) < f(\rho^-)$.

If instead $\rho^- > \rho^+$, then $f'(\rho^-) < f'(\rho^+)$ and so the entropy-admissible solution to the Riemann problem is given by the rarefaction wave

$$\rho(x,t) = \begin{cases} \rho^- & \text{if } x < f'(\rho^-)t \\ (f')^{-1}(\frac{x}{t}) & \text{if } f'(\rho^-)t < x < f'(\rho^+)t \\ \rho^+ & \text{if } x > f'(\rho^+)t. \end{cases} \tag{14}$$

3 Numerical scheme

The numerical algorithm we use to simulate the behaviour of the traffic flow is the Godunov scheme, which is a conservative finite-volume method that solves exact or approximate Riemann problems at each inter-cell boundary, suggested by S. K. Godunov in 1959. Hereafter we give the most important features of the scheme, for more details see [Godunov 1959] and [Piccoli Garavello 2006].

3.1 Numerical grid

A numerical grid has been defined using the following notations:

- Δx is the space grid size,
- Δt is the time grid size,
- $(x_m, t_n) = (m\Delta x, n\Delta t)$ are the grid points.

For a function defined on the grid we write $v_m^n = v(x_m, t_n)$ for m, n varying on a subset of $\mathbb{Z}$ and $\mathbb{N}$ respectively.

3.2 Godunov scheme

The idea underlying Godunov scheme is the following:

1. the initial datum is approximated by a piecewise constant function

$$v_m^0 = \frac{1}{\Delta x} \int_{x_m - \frac{1}{2}\Delta x}^{x_m + \frac{1}{2}\Delta x} u_0(x)\mathrm{d}x, \quad m \in \mathbb{Z} \tag{15}$$

2. the corresponding Riemann problems are solved exactly and a global solution is simply obtained by piecing them together: if we call v^Δ the exact solutions at points $\left(m - \frac{1}{2}\right)$, $m \in \mathbb{Z}$ then the projection of the solution is defined as

$$v_m^{n+1} = \frac{1}{\Delta x} \int_{x_m - \frac{1}{2}\Delta x}^{x_m + \frac{1}{2}\Delta x} v^\Delta(t_{n+1}, x)\mathrm{d}x \tag{16}$$

3. one takes the mean and proceeds by induction on every t_n.

Under the CFL condition,

$$\Delta t \sup_{m,n} \left\{ sup_{u \in I(u_m^n, u_{m+1}^n)} |f'(u)| \right\} \leq \Delta x \tag{17}$$

the waves, generated by different Riemann problems, do not interact.

We can use the Gauss-Green formula to compute v^{n+1} and the flux in $x = x_m - \frac{1}{2}\Delta x$ for $t \in (t_n, t_{n+1})$ is given by

$$f(u(t, x_m - \frac{1}{2}\Delta x)) = f(W_R(0; v_{m-1}^n, v_m^n)), \tag{18}$$

where $W_R(\frac{x}{t}; v_-, v_+)$ is the self-similar solution between v_- and v_+. Similarly for the point $x = x_m + \frac{1}{2}\Delta x$:

$$f(u(t, x_m + \frac{1}{2}\Delta x)) = f(W_R(0; v_m^n, v_{m+1}^n)). \tag{19}$$

As the flux is time invariant and continuous, we can put it out of the integral and, setting

$$g^G(u, v) = f(W_R(0; u, v)) \tag{20}$$

under the condition (17), the scheme can be written as

$$v_m^{n+1} = v_m^n - \frac{\Delta t}{\Delta x} \left(g^G(v_m^n, v_{m+1}^n) - g^G(v_{m-1}, v_m^n) \right). \tag{21}$$

The expression of the numerical flux for Godunov method is in general given by

$$g^G(u, w) = \begin{cases} min_{z \in [u,w]} f(z) & \text{if } u \leq w \\ max_{z \in [w,u]} f(z) & \text{if } w \leq u \end{cases} \tag{22}$$

As we supposed f to be concave, (22) is equivalent to

$$g^G(u, w) = min(D(u), S(w)) \tag{23}$$

where

$$S(u) = \begin{cases} f_{max} & \text{if } u \leq \rho_c \\ f(u) & \text{if } u \geq \rho_c \end{cases} \tag{24}$$

and

$$D(u) = \begin{cases} f(u) & \text{if } u \leq \rho_c \\ f_{max} & \text{if } u \geq \rho_c \end{cases}. \tag{25}$$

Above, ρ_c is the critical density and f_{max} the maximum of the f function. D is called demand and S supply. These functions have been introduced by J.P. Lebacque in [Lebacque 1996]. The demand function measures the maximum flux that an incoming road may demand to send, while the supply function measures the maximum flux that an outgoing road may supply space for.

In the case of a flux function that presents a capacity drop, a small correction must be made, see [Wiens Stockie Williams 2013]. In particular, we set

$$\begin{array}{ll}
\text{if } u_j < u_c & D(u_j) = \min(f(u_j), f_c(u_c)) \\
\text{if } u_j > u_c & D(u_j) = f_f(u_c) \\
\text{if } u_j = u_c & \text{if } u_{j+1} < u_c \, D(u_j) = D(u_c) = f_f(u_c) \\
. & \text{if } u_{j+1} > u_c \, D(u_j) = D(u_c) = f_c(u_c) \\
\text{if } u_{j+1} < u_c & S(u_{j+1}) = f_f(u_c) \\
\text{if } u_{j+1} > u_c & S(u_{j+1}) = f(u_{j+1}) \\
\text{if } u_{j+1} = u_c & \bar{l} = \min\{l : j+1 < l \leq N \text{ and } u_l \neq u_c\} \\
 & \text{if } u_{\bar{l}} < u_c \, S(u_{j+1}) = S(u_c) = f_f(u_c) \\
 & \text{if } u_{\bar{l}} > u_c \, S(u_{j+1}) = S(u_c) = f_c(u_c) \\
 & \text{if } \nexists \bar{l} \quad S(u_{j+1}) = S(u_c) = f_f(u_c) \\
\text{if } u_j = u_{j+1} = u_c & D(u_j) = S(u_{j+1})
\end{array} \tag{26}$$

3.2.1 Boundary conditions

Suppose to have the Cauchy problem

$$\begin{array}{l}
u_t + f(u)_x = 0 \\
u(x,0) = u_0(x) \quad x \geq 0
\end{array} \tag{27}$$

and to assign a condition at the incoming boundary $x = 0$

$$u(0,t) = u_0(t) \quad t \geq 0 \ . \tag{28}$$

It is not always possible to find a function u that satisfies (28) in a classical sense, because, in general, the boundary data cannot be assumed. One seeks a condition which is to be effective only in the inflow part of the boundary. The rigorous way to assign the boundary condition is

$$\max_{k \in I(u(0,t), u_0(t)} \{\text{sgn}(u(0,t) - u_0(t))[F(u(0,t)) - F(k)]\} = 0, \tag{29}$$

see [Bardos Le Roux Nédélec 1979]. With regard to the implementation of the numerical scheme, we then have three ways of assigning boundary conditions:

1. We add two ghost cells, at the beginning and at the end of the space grid. Their indexes are 0 and $M+1$ respectively. We assign the value of density in these cells:

$$\begin{array}{ll}
u_0(t) = U_0(t) & \text{for } t \geq 0 \\
u_{M+1}(t) = U_{M+1}(t) & \text{for } t \geq 0
\end{array} \tag{30}$$

At the inflow part of the boundary we define

$$v_1^{n+1} = v_0^n - \frac{\Delta t}{\Delta x} \left(g^G(v_1^n, v_2^n) - g^G(v_0^n, v_1^n) \right) \tag{31}$$

where

$$v_0(t) = \frac{1}{\Delta t} \int_{t_n}^{t_{n+1}} U_0(t) \mathrm{d}t \tag{32}$$

The outgoing boundary is treated analogously.

$$v_N^{n+1} = v_N^n - \frac{\Delta t}{\Delta x} \left(g^G(v_N^n, v_{N+1}^n) - g^G(v_{N-1}^n, v_N^n) \right) \tag{33}$$

where

$$v_{N+1}^n(t) = \frac{1}{\Delta t} \int_{t_n}^{t_{n+1}} U_{M+1}(t)\mathrm{d}t \tag{34}$$

2. We assign the flux at boundaries

$$\begin{array}{ll} f(u(t, x_1 - \frac{1}{2}\Delta x)) = F_{in}(t) & \text{for } t \geq 0 \\ f(u(t, x_{M+1} + \frac{1}{2}\Delta x)) = F_{\text{out}}(t) & \text{for } t \geq 0 \end{array} \tag{35}$$

and then compute the corresponding numerical flux at $x_1 - \frac{1}{2}\Delta x$ and $x_{M+1} + \frac{1}{2}\Delta x$ as

$$\begin{array}{ll} g^G(v_0^n, v_1^n) = \min(F_{\text{in}}^n, S(v_1^n)) & n = 1, ..., N \\ g^G(v_M^n, v_{M+1}^n) = \min(D(v_M^n), F_{\text{out}}^n) & n = 1, ..., N \end{array} \tag{36}$$

3. We just observe that boundary conditions become uninfluential in points quite far from the boundaries, because there the density depends only on what happens in the considered road segment (at least for a certain time). We assume absorbing boundary conditions in $x = x_{\text{entry}}$ and $x = x_{\text{exit}}$: two ghost nodes are added at the beginning and at the end of the road and we set $\rho_0^n = \rho_1^n$ and $\rho_{M+1}^n = \rho_M^n$.

3.2.2 Conditions at junctions

On-ramps: We call $F_{\text{on}}(t)$ the flux of cars that is running in the on ramp located at interface $j + \frac{1}{2}$, we want to understand how this influences the flux $F_{j+\frac{1}{2}}$.

If cell $j + 1$ can meet the demand of cell j plus that of the ramp, then the outgoing flux of cell j will be equal to his demand, while the incoming flow of cell $j + 1$ will be the sum of the 2 demands. Thus, we have to distinguish the two fluxes: from now on, we will call $F_{j+\frac{1}{2}}^-$ the outgoing flux of cell j and $F_{j+\frac{1}{2}}^+$ the incoming flux of cell $j + 1$. Now we can write

$$\begin{array}{ll} \text{if} & \min(D(v_j) + F_{\text{on}}, S(v_{j+1})) = D(v_j) + F_{\text{on}} \\ \text{then} & F_{j+\frac{1}{2}}^- = D(v_j) \\ & F_{j+\frac{1}{2}}^+ = D(v_j) + F_{\text{on}} \end{array} \tag{37}$$

On the contrary, if the supply of cell $j + 1$ is smaller than the sum of the two demands, we have introduce a right of way parameter, q, that indicates which portion of cars that are already in the highway and cars that want to enter will fill cell $j + 1$.

$$\begin{array}{ll} \text{if} & \min(D(v_j) + F_{\text{on}}, S(v_{j+1})) = S(v_{j+1}) \\ \text{then} & F_{j+\frac{1}{2}}^- = (1 - q)S(v_{j+1}) \\ & F_{j+\frac{1}{2}}^+ = S(v_{j+1}) \end{array} \tag{38}$$

Off-ramps: In the case of off-ramps, we consider that all cars can exit the highway, then the resulting fluxes are

$$\begin{array}{l} F_{j+\frac{1}{2}}^- = \min((1 - \alpha)D(v_j), S(v_{j+1})) + \alpha D(v_j) \\ F_{j+\frac{1}{2}}^+ = \min((1 - \alpha)D(v_j), S(v_{j+1})) \end{array} \tag{39}$$

where α is the portion of cars in cell j that want to exit the highway.

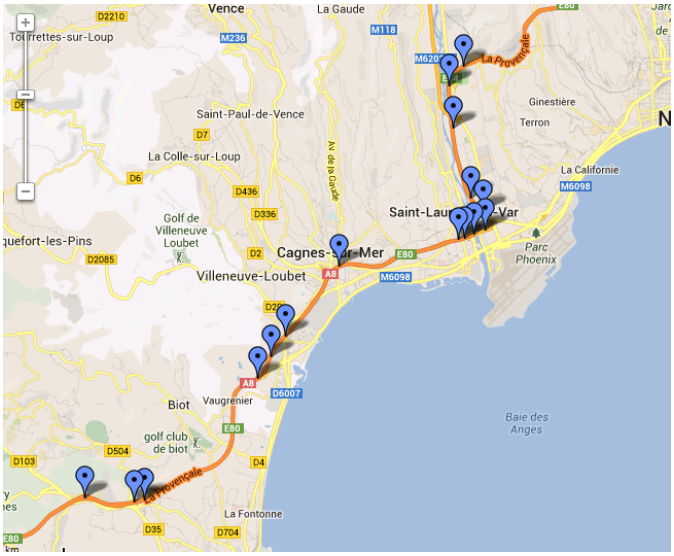

Figure 6: The considered part of the A8 highway

4 Experimental data

4.1 *La Provençale*

Data provided from the two partners correspond to a part of the A8 highway, also called *la Provençale*, that links Aix-en-Provence and the A7 highway to the Côte d'Azur. The part under consideration spans from exit 45 (Antibes) to exit 49 (Nice St Isidore) for a total of 17,5 km, see Fig. 6. The whole portion is in general highly congested, and long queues are usual.

Data concern both directions. From now on, we will call *Direction 1* the one that goes from Antibes to Nice St Isidore, *Direction 2* the opposite one.

The discretization of the highway into cells (see Section 3.1) has been done such that the speed limit and the number of lanes is constant on each cell, all cells are approximately 200 m long and all on and off ramps are located at interfaces between two cells. This criteria lead to a subdivision in 89 cells per direction. The resulting repartition into cells is given in Tables 1 and 2.

4.2 Raw data

Traffic data available for the project were collected on four Tuesdays (March 19 and 26 and April 2 and 9, 2013) from 6 a.m. to 11 a.m. and are mainly divided into two categories:

GPS data provided by the company Autoroutes Trafic which correspond to data supplied by Coyote systems, of which we discuss in more detail in Section 4.3. Each observation includes the position and the velocity of the car, as well as its ID. The percentage of cars equipped with GPS is estimated to represent approximately 2% (see Section 4.5) of the total volume of traffic, and each GPS sends data every minute, so that we have between 8000 and 10000 measurements per day. In traffic engineering literature (see [Treiber Kesting 2013]), these data are classified as *trajectory data* and, in particular, they are called *extended floated-car data* (xFCD), which is the term that indicates data coming from GPS receivers equipped with *extra* sensors, such as the

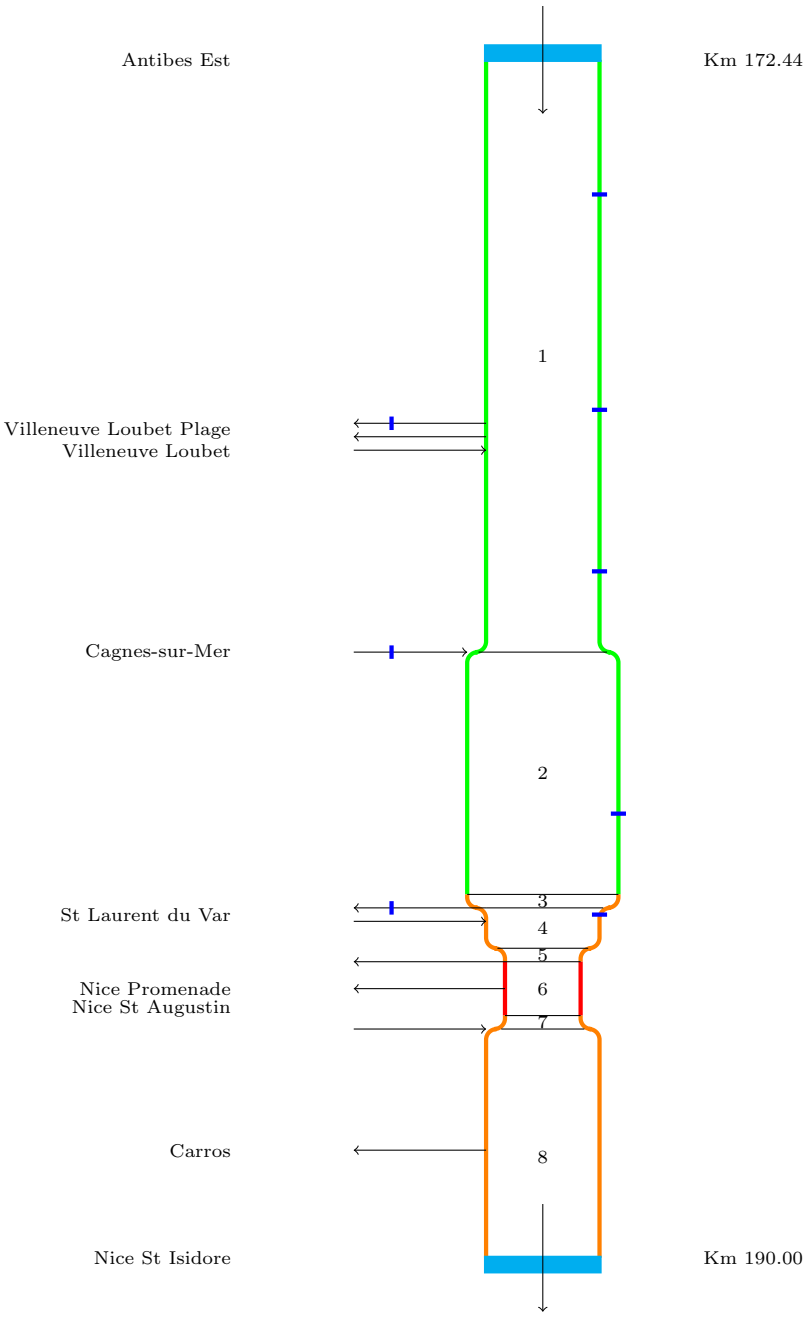

Figure 7: Highway's scheme. Direction 1. Blue spots indicate loop detectors' locations. Light blue lines indicate toll stations' locations. Black arrows indicate the direction of cars flow, where those on the left are on and off ramps. Highway's sections limited by green lines are those where the speed limit is 100 kilometers per hour, while in the orange ones is 90 and in the red one is 70 kilometres per hour. Width is proportional to the number of lanes: 2, 3 or 4.

Subset	Cells	Speed limit	Number of lanes	Km_{min}	Km_{max}
1	1 to 44	110	3	172.44	181.20
2	45 to 62	110	4	181.20	184.70
3	63	90	4	184.70	184.97
4	64 to 66	90	3	184.97	185.60
5	67	90	2	185.60	185.80
6	68 - 69	70	2	185.80	186.20
7	70 to 72	90	2	186.20	186.76
8	73 to 89	110	3	186.76	190.00

Table 1: Discretization. Direction 1

Subset	Cells	Speed limit	Number of lanes	Km_{min}	Km_{max}
1	1 to 18	110	2	190.00	186.50
2	19	90	2	186.50	186.32
3	20 - 21	90	2	186.32	185.97
4	22	90	2	185.97	185.80
5	23 - 24	90	3	185.80	185.40
6	25 - 26	90	4	185.40	185.00
7	27 to 45	110	4	185.00	181.23
8	46 to 89	110	3	181.23	172.47

Table 2: Discretization. Direction 2

one that records the vehicle speed, as in our case. These data have been used both to constantly feed the algorithm by experimental data and to compare the numerical results at the end of the simulation. In Fig. 8 we report in the space-time plane all the registered data on March 19^{th}.

Inductive-loop vehicle detectors' data provided by the highway operator *VINCI Autoroutes*. These are static sensors installed beneath the road surface located at toll stations and some other strategic locations along the highway. They fall under the category of cross-sectional data, as they measure the number of cars passing through a fixed cross-section on the road. This kind of data is usually represented in time series of some aggregated quantity like we have done for flux in Fig. 13. Traffic flow is easily derived from such values as $f = \frac{\Delta N}{\Delta t}$ where ΔN is the value provided by the induction loops and Δt is the time interval at which we make the average. They are necessary for the estimation of the real amount of cars travelling on the considered section and also represent an ulterior support to the validation of the model. Both the flux averages over one hour and six minutes have been provided.

4.3 The *Coyote* system

Data used for the project are those sent by Coyote radars. Coyote is a European system that warns users about the location of *dangerous* areas through the exchange of information entered by users, through the GSM network. The system is based on a process of sharing information by members in order to prevent each others of the presence of a radar, a disturbance or an accident on the way as soon as it is *spotted* on the road. The user that wants to warn the other simply presses a key on the screen so that his position is detected by Coyote and is transmitted via

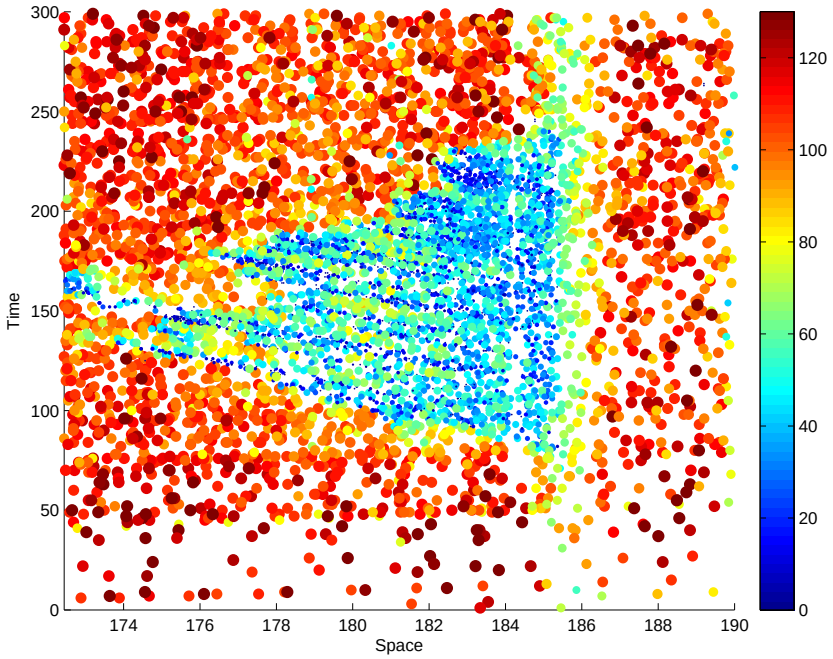

(a) Direction 1

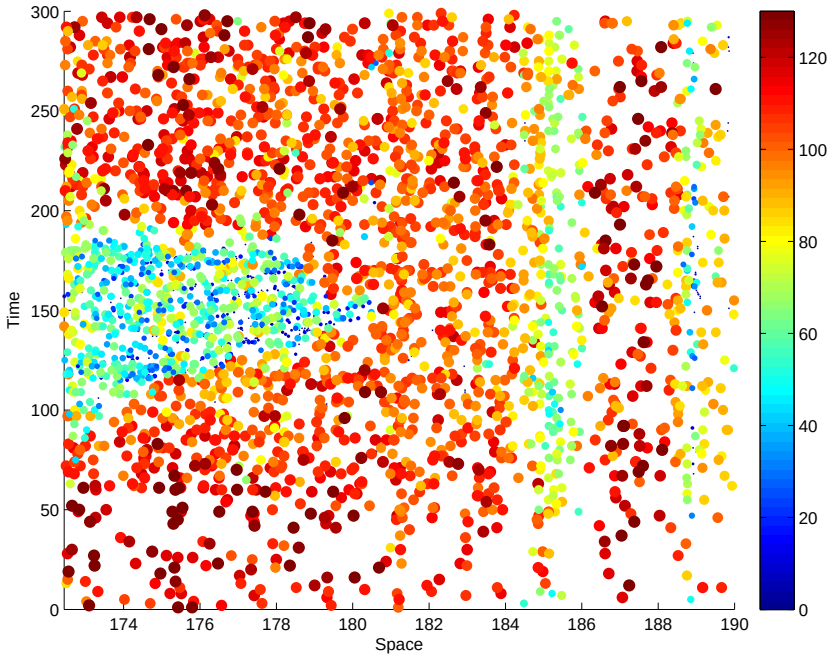

(b) Direction 2

Figure 8: GPS data of March 19$^{\text{th}}$.
Spots sizes are proportional to speed.

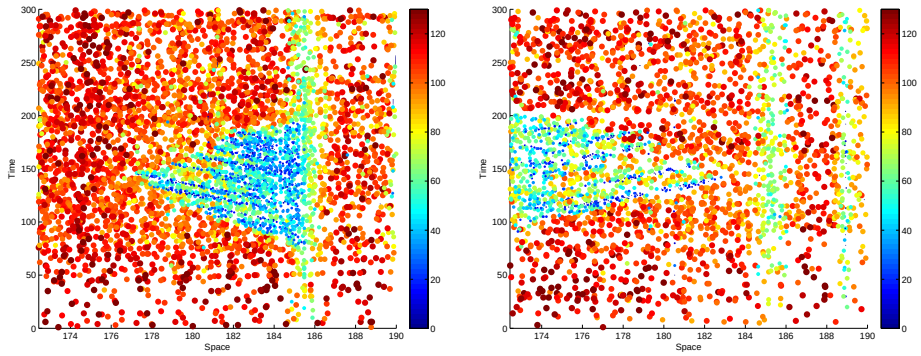

(a) Direction 1 (b) Direction 2

Figure 9: GPS data of March 26$^{\text{th}}$.

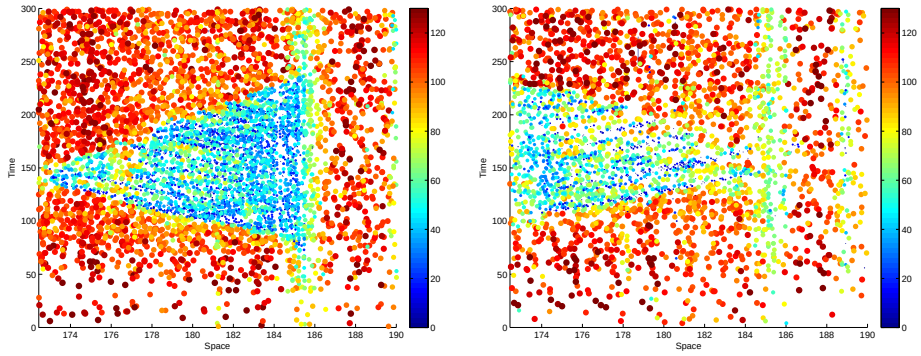

(a) Direction 1 (b) Direction 2

Figure 10: GPS data of April 2$^{\text{nd}}$.

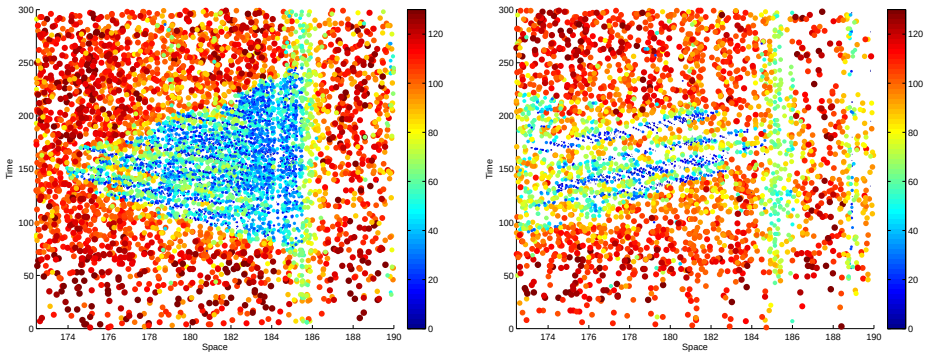

(a) Direction 1 (b) Direction 2

Figure 11: GPS data of April 9$^{\text{th}}$.

Figure 12: A Coyote radar

the GSM network to update a common database. The system is then capable of giving drivers a lot of informations about traffic conditions such as traffic light and mobile camera locations, speed limits, traffic incidents and more. Of course, the quality of information is related mainly to the freshness of the information, and therefore dependent on the seriousness and the number of service users. These systems are sometimes integrated with GPS. Its built-in GSM/GPRS modem constantly communicates with the Coyote servers to send drivers the right information at the right time, according to the location and speed of their vehicle.

4.4 Data processing

GPS data had been previously treated by *Autoroutes Trafic*, who selected the data related to the considered stretch of highway and repositioned them in the best way. The files they provided were `.csv` files containing, for each observation, the GPS ID, the day and hour when the signal was sent from the GPS, the speed of the car at that time, its position expressed as latitude, longitude and orientation, direction (1 or 2) in which it was travelling, the section of the highway where it was and percentage that it already covered. Knowing the starting kilometer of each road section, it has been possible, using the percentage, to compute the position of each car.

GPS data had then been used in order to compute:

Fluxes at boundaries at km x have been computed counting the number of probe cars passing between km x and km $x + 2.5$ each minute. These values, multiplied by 60, give the flux in cars per hour. More details about this computation are given in Algorithm 1.

On the contrary, *VINCI Autoroutes*' data were ready to use. The given values have been considered to be constant during all the 6 minutes (or 1 hour) of the measurement. An example is shown in Fig. 13.

Ghost cells densities To obtain these values, the average velocities of all the observations over one minute in the chosen 0 and $M + 1$ cells have been computed. Then, the corresponding density has been found according to the velocity function in use.

Approximated real values The estimated speed field, i.e. the continuous function of local speed average $v(x, t)$, has been derived from the discrete GPS measurements as the ghost cells densities, the only difference is that the average of velocities is computed on 2 consecutive cells and 6 consecutive minutes and all over the space-time grid. An example is given in Fig. 14a. They will be compared with the simulation results to verify the goodness of the model.

Data: .xslx files of GPS data
Result: .csv file containing flux at each minute from 6am to 11am

choose km x, day and direction at which compute the flux;
load data of the corresponding day from excel file;
if *direction 1* **then**
  control zone goes from km x to km x + 2.5;
else
  control zone goes from km x to km x - 2.5;
end
create a sorted list of minutes in excel format;
create an empty flux vector of the same size;
create an empty vector of car IDs;
if *data belongs to the control zone and the chosen direction and the car's ID isn't in the list of counted IDs* **then**
  increment the flux of 1 unit at the position of the corresponding minute;
  add the car's ID to the list of counted IDs;
end
multiply the flux by 60;
make the average of flux over 5 minutes;

Algorithm 1: Compute fluxes at boundaries from GPS data

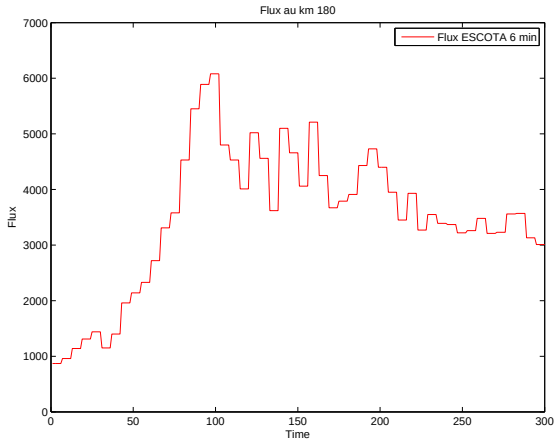

Figure 13: Loop detectors' data at km 180, March 19th direction 1.

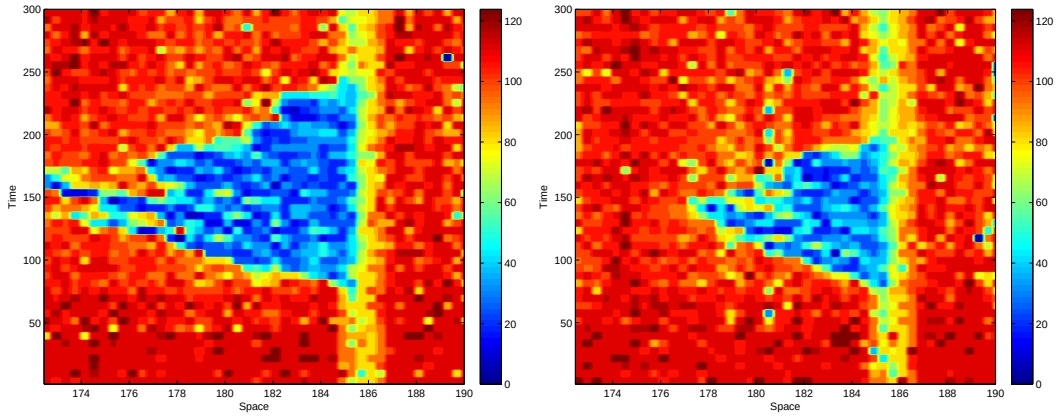

(a) March 19$^{\text{th}}$, direction 1.

(b) March 26$^{\text{th}}$, direction 1.

(c) April 2$^{\text{nd}}$, direction 1.

(d) April 9$^{\text{th}}$, direction 1.

Figure 14: GPS average data

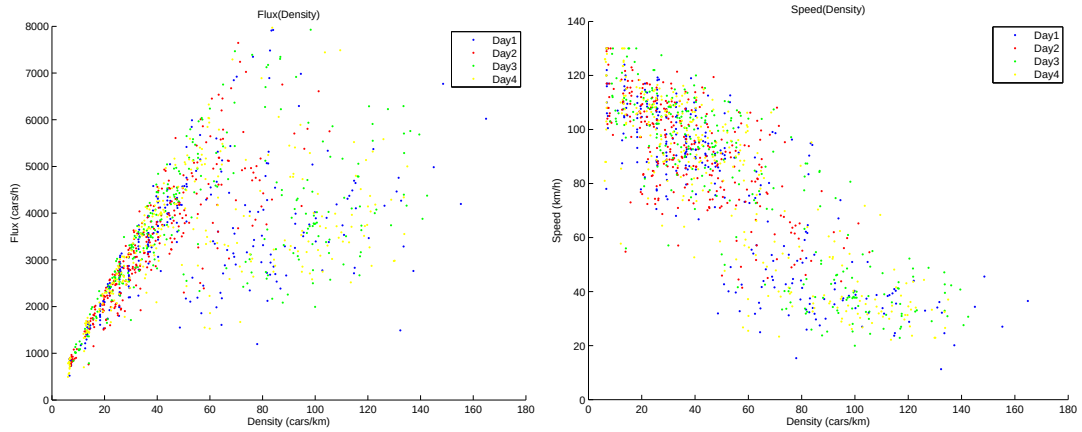

(a) Flux - density (b) Speed - density

Figure 15: Data used for parameter calibration

Data used for parameter calibration Data used for parameter calibration are the averages over one minute and a whole subset of cells of tables 1 and 2 of densities, velocities and flux. In particular, we call `k` the ID of the considered subset of cells (see the first column of tables 1 and 2), `nkj` the number of cars that are in subset k at minute j, `vkj` the average speed of cars in subset k at minute j, `ki` the starting kilometer of the considered highway portion, `kmf` the ending kilometer of the considered highway portion, `Nobs` the total number of observations. The minute number `j` is counted starting from 6.00 a.m. which corresponds to minute 1 and goes up to 300.

First of all, we compute the total number of cars equipped with a Coyote system which occupy the considered portion during minute `j` in the subset of cells named `k`. From this we can derive the density, the average speed and, of course, the flux.

```
% Number of cars
for i=1:Nobs
        if t(i)==j && km(i)>kmi && km(i)<kmf
                nkj = nkj+1;
                vkj = vkj + v(i);
        end
end

% Density
dkj = nvk(kmi-kmf);

%Average speed
vkj = vkj / nkj;

%Flux
fkj = dkj * vkj;
```

These values are then scaled with percentages listed in Section 4.5. We obtain, for the subset 1 of the Antibes-Nice direction, which is composed by the first 44 cells, the points shown in Fig. 15.

The sparseness of data is due to several factors: the varying percentage of trucks at different times of the day, different weather conditions (lighting, precipitations), etc. Moreover, the relation $f = \rho v$, which is the foundation of the LWR model, assumes that traffic flow and speed

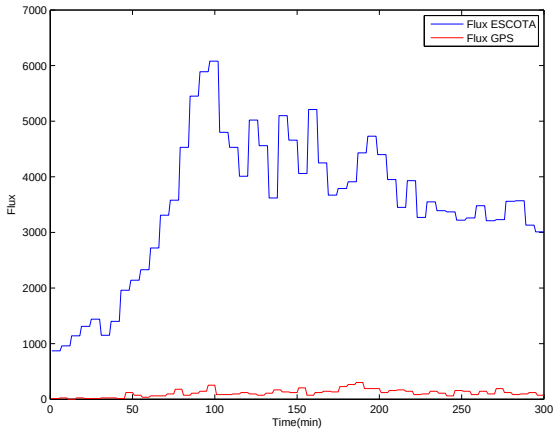

Figure 16: Loop detectors and GPS data at km 180. March 19$^{\text{th}}$, direction 1.

Day	6-7 a.m.	7-8 a.m.	8-9 a.m.	9-10 a.m.	10-11 a.m.
1	1.38 %	1.73 %	2.66 %	2.95 %	2.91 %
2	1.36 %	1.74 %	2.31 %	3.00 %	2.28 %
3	0.88 %	1.70 %	2.30 %	2.30 %	2.18 %
4	1.12 %	1.70 %	2.61 %	2.60 %	2.14 %

Table 3: Incoming flux percentage. Km 180, direction 1

are always in local equilibrium with respect to the density, i.e. they simultaneously follow the density, not only for steady-state traffic but in all situations, which is not always the case.

4.5 Data percentage

Knowing both the values of GPS and loop detectors' fluxes, allowed us to compute the percentage of cars equipped with GPS with respect to the total amount of cars. This has been done by comparing the sum of the 1 hour values of loop detectors' flux at the toll stations of Antibes Est, Antibes West and Sophia Antipolis to the average GPS flux over one hour just after the last of these three toll stations. Notice that there are no off ramps in the considered part and that Antibes Est toll station counts all the cars that are travelling on the highway, while the others two count those who are entering in the Antibes area, so the sum of cars that pass through these three toll stations corresponds to the exact entering flux (unless there are some errors in the counting). An example of visual comparison is given in Fig. 16. All the percentages per hour and per day are collected in Table 3.

As we can easily see, the percentage of available data is not constant during the day, but it has the same pattern every day: early in the morning the percentage of cars equipped with a Coyote system is very low (0.9-1.4%), then it starts growing until it reaches the maximum between 9 and 10 a.m. (2.3-3%). Finally it starts decreasing again. This is probably due to the fact that Coyote systems are mainly used by some specific categories of people such as taxi or truck drivers. Data suggest that the presence of this kind of vehicles is regular and is not proportional to the total number of cars.

As we wanted to estimate the real amount of cars that were travelling along the highway at any time and at any point of the considered stretch from the Coyote data, we used a linear

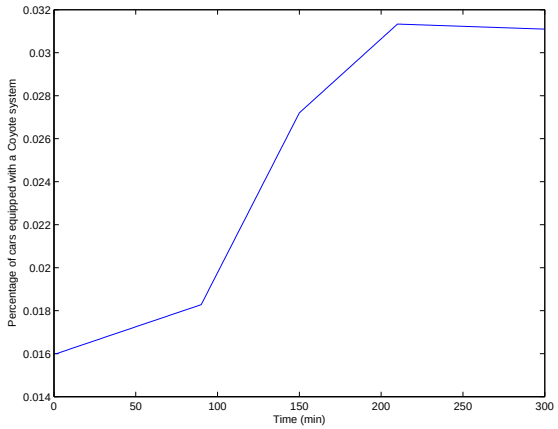

Figure 17: Percentages interpolation. March 19$^{\text{th}}$, direction 1.

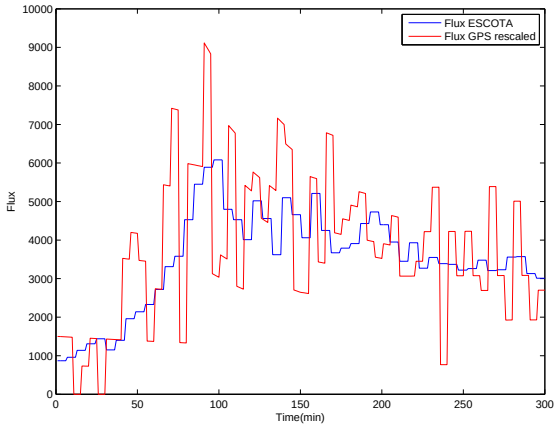

Figure 18: Loop detectors data (6 minutes average) and GPS data after rescaling according to the interpolated percentages. March 19$^{\text{th}}$, direction 1.

interpolation of the percentages obtained before in order to rescale the GPS data. To do this, we computed the value of the interpolation at each minute and assigned it to the corresponding GPS flux obtained as explained in Section 4.4. This allowed us to rescale each flux with a percentage as precise as possible. We report in Fig. 17 the percentage interpolation and in Fig. 18 the comparison between LD data and rescaled GPS data for March 19th.

5 Parameters calibration

Data obtained as explained in Section 4 have been used in order to calibrate the model parameters. Calibration is the estimation of parameters to maximize the model's descriptive power to reproduce collective traffic-flow characteristics. The chosen fundamental diagrams are modified Daganzo-Newell (Fig. 4) and modified Daganzo-Newell with capacity drop (Fig. 5). For each cell, all five parameters of the flux function: $v_{max}, \rho_{max}, \omega_f, \rho_a$ and ρ_c and the *critical* speeds (speeds corresponding to the critical density, one or two depending if we assume that there's a

capacity drop or not) have to be determined from experimental data.

5.1 Least squares regression

We make the calibration for each subset of cells that have the same speed limit and number of lanes. Data used for the calibration are those obtained as explained in Section 4.4.

Given the shape of the function $v(\rho)$, we decided to split the calibration in two subsequent parts: first we use Matlab's `polyfit` function to do the linear regression on the non-congested set, then we find the other parameters with the `nlinfit` command, that uses the Levenberg-Marquardt algorithm. The advantage of this method is that it tries to combine the advantages of the gradient descent (robustness) and Gauss-Newton (fast convergence) by making a smooth transition between these methods during optimization. The transition is governed by an adaptive *trust region* preventing the Gauss-Newton method from stepping *too far*. This is the most popular method for standard problems of calibration.

```
% Data loading
load('x')  % Vector of densities
load('y')  % Vector of the corresponding speeds

% Selection of uncongested data
xNC = [];
yNC = [];

for j=1:max(size(y))
    if y(j)>=vv(i)
        yNC = [yNC y(j)];
        xNC = [xNC x(j)];
    end
end

% First regression
p= polyfit(xNC, yNC, 1);

vmax(i) = p(2);
rhoa(i) =  -vmax(i)/p(1);
rhoc(i) = (vmax(i) - vv(i))*(rhoa(i)/vmax(i));

% Selection of congested data
xC = [];
yC = [];

for j=1:max(size(y))
    if y(j)<vv(i)
        yC = [yC y(j)];
        xC = [xC x(j)];
    end
end

% Second regression
beta0 = 100;
r2 = @(b, x)(x<=rhoc(i)).*(p(2)+p(1).*x)+...
     ...(x>rhoc(i)).*(b./x+vv1(i)-b./rhoc(i));
mdl = nlinfit(xC,yC, r2, beta0);

omegaf(i) = - vv(i) + mdl/rhoc(i);
rhomax(i) = mdl/omegaf(i);
```

For the critical speed, we first tried to choose it by computing the residual sum of squares of the interpolation with different critical speeds and taking the one that gave the minimal RSS,

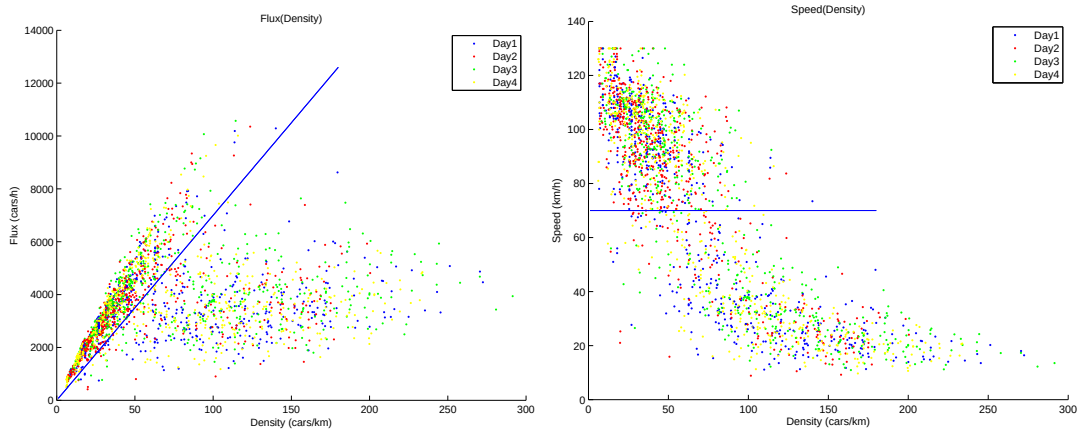

(a) Flux - density (b) Speed - density

Figure 19: Critical speed

see Algorithm 2. We had to abandon this technique because data are so sparse that the RSS turned out to be a misleading indicator.

vv = 60:0.05:100;
for *Each value of vv* **do**
  Make the two regressions as before;
  Compute the residual sum of squares;
end
Choose the critical speed that produces minimal RSS;

Algorithm 2: Find the value of vv that minimizes the error

We then decided to choose the critical speed according to a simple visual criterion. In fact, in the speed-density plot, it can be easily noticed that data are divided in two parts, that we considered as the congested and uncongested set of data . For the first subset of cells, the critical density chosen in this way is $v_{lim} = 70km/h$ (see Fig. 19). For the fundamental diagram with capacity drop, the values of v_{lim1} and v_{lim2} have been chosen by looking at the velocities histogram, reported in Fig. 20. It has been easy to understand from it which velocities appear rarely. Then, the same kind of regression as for the first fundamental diagram has been used.

The results for the first subset in the Antibes-Nice direction, the longest one, that includes 44 cells, are shown in Fig. 21a and 21b, corresponding to the modified Daganzo-Newell fundamental diagram with and without capacity drop. The method exposed just before can't be applied to the smallest subsets of homogeneous cells, i.e. subsets 3 to 8. Problems arise because of the excessive sparseness of data. The issue has been overcome by extrapolating a linear trend in parameters linked to the theoretical speed limit and the number of lanes from the sections where the regression could be performed. Thanks to the so obtained coefficients we have been capable of estimating parameters for every cell, knowing only their characteristics. The identified parameters are listed in Tables 4 and 5.

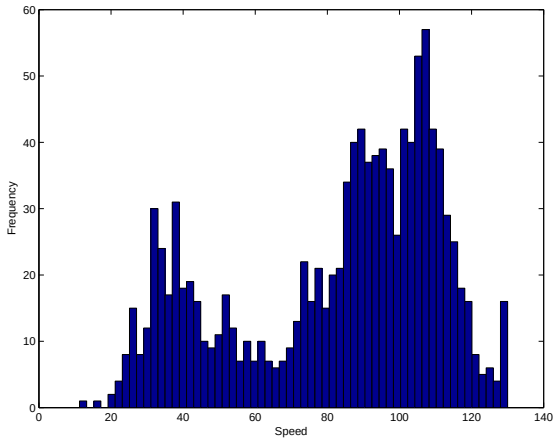

Figure 20: Velocities histogram

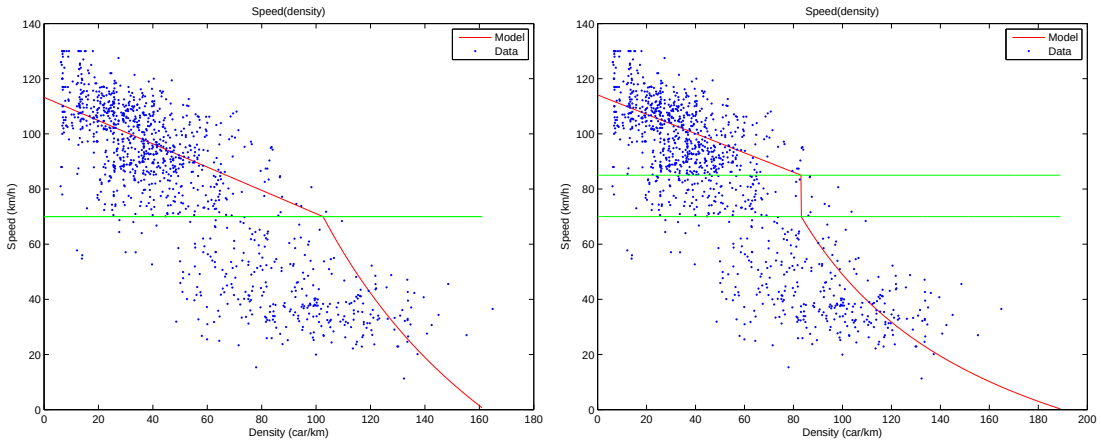

(a) Hyperbolic-linear fundamental diagram.

(b) Hyperbolic-linear fundamental diagram with capacity drop.

Figure 21: Parameter calibration for the homogeneous section from km 172.44 to 181.2 (Antibes-Nice).

Subset #	ρ_{max} (car/km)	v_{lim} (km/h)	ρ_a (car/km)	ρ_c (car/km)	v_{max} (km/h)	ω_f (km/h)
1	165.83	70.00	313.22	118.86	112.81	177.16
2	248.18	70.00	462.96	176.04	112.95	170.83
3	329.40	57.27	598.96	227.52	92.35	127.91
4	247.05	57.27	449.22	170.65	92.35	127.91
5	247.05	57.27	449.22	170.65	92.35	127.92
6	164.70	57.27	299.48	113.76	92.35	127.92
7	247.05	57.27	449.22	170.65	92.35	127.92
8	247.05	70.00	449.22	170.65	112.88	156.34

Table 4: Linear regression and extrapolation results without capacity drop. Direction 1

Subset #	ρ_{max} (car/km)	v_{lim1} (km/h)	v_{lim2} (km/h)	ρ_a (car/km)	ρ_c (car/km)	v_{max} (km/h)	ω_f (km/h)
1	182.27	70.00	85.00	389.87	98.00	113.54	81.40
2	237.63	70.00	85.00	559.88	145.55	114.86	110.65
3	221.44	57.27	69.55	680.04	173.88	93.44	209.39
4	166.08	57.27	69.55	510.03	130.41	93.44	209.39
5	110.72	57.27	69.55	340.02	86.94	93.44	209.39
6	110.72	44.55	54.09	340.02	86.94	72.67	162.86
7	110.72	57.27	69.55	340.02	86.94	93.44	209.39
8	166.08	70.00	85.00	510.03	130.41	114.20	255.93

Table 5: Linear regression and extrapolation results with capacity drop. Direction 1

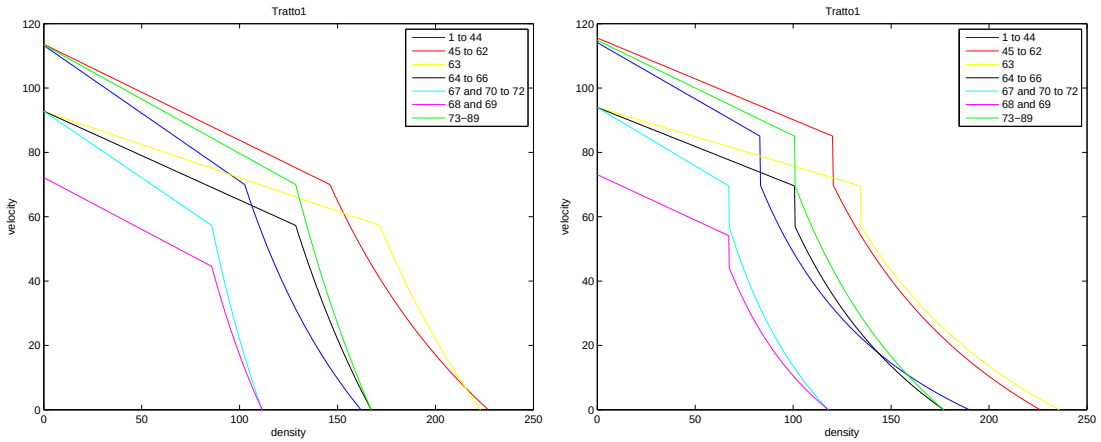

(a) Hyperbolic-linear fundamental diagram.

(b) Hyperbolic-linear fundamental diagram with capacity drop.

Figure 22: Parameter calibration result, direction 1.

5.2 L^1 error

The second method is the one proposed in [Blandin et al. 2013]. It consists in comparing the time-space diagrams derived from the experimental data presented in Section 4.4 with the simulation results. To do this, we define the following cost function

$$L^1(u) = \frac{\sum_n \sum_j |u_{sim}(n\Delta t, j\Delta x) - u_{data}(n\Delta t, j\Delta x)|}{\sum_n \sum_j |u_{data}(n\Delta t, j\Delta x)|} \tag{40}$$

in which we note $u_{data}(n\Delta t, j\Delta x)$ the average density computed from data as described in Section 4.4 on 2 cells and 6 minutes and $u_{sim}(n\Delta t, j\Delta x)$ the average on the same grid of the numerical value of ρ. Then we run the simulation with different parameters and try to identify the set of parameters at which the minimum of the cost function is attained for the reconstructed time-space diagrams.

We chose to evaluate the cost function on all the points of a grid with parameters *gapvector*, *vmaxvector*, *rcvector* in Algorithm 3. The other parameters are those identified in Section 5.1. This choice of the parameters allows us to *move* all the parts of the fundamental diagram in the $(\rho - v(\rho))$ space maintaining some points of reference that we consider as plausible.

Data: A set of plausible parameters
Result: Best parameters

```
gapvector = [15 10 5 0];
vmaxvector = [105 109 113 117 121 125];
rcvector = [70 75 80 85 90 95 100 105 110 115 120];
for All values in gapvector do
    for All values in vmaxvector do
        for All values in rcvector do
            Run simulation;
            Compute error;
        end
    end
end
Choose parameters that produce minimal error;
```

Algorithm 3: Find parameters that minimize the error

To this end, we use data of April 2$^{\text{nd}}$, when the best-shaped traffic profile has been recorded. We obtain, for subset 1, $\rho_{max} = 241.01$ car/km, $v_{lim1} = 70$ km/h, $v_{lim2} = 85$ km/h, $\rho_a = 484.26$ car/km and $\rho_c = 120$ car/km, $v_{max} = 113$ km/h and $\omega_f = 54.54$ km/h.

Values for the second subset can be obtained by keeping the first ones fix and doing the same optimization running the simulation on subsets 1 and 2 together.

5.3 Graphical estimation

Another way of estimating parameters is to derive some of them directly from the data scatterplots. In fact, in Fig. 8, 9, 10 and 11, we can easily recognize ω_f, which is the speed of propagation of the congestion wave, and the slopes that correspond to the shocks produced by the formation and the extinction of the traffic jam, that in the fundamental diagram of Fig. 23 correspond to lines 1 and 2 respectively. These three values have been measured from data as shown in Fig. 24a and 24b. We find $\omega_f = 17$ km/h, $s_1 = 8.85$ km/h and $s_2 = -14.06$ km/h.

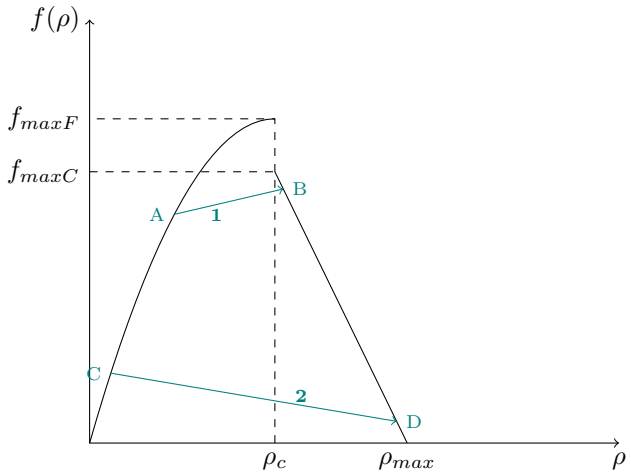

Figure 23: Shocks corresponding to queue formation and extinction waves

From the previous chapter, we can suppose that, in subset 1, $v_{lim1} = 70$ km/h, $v_{lim2} = 85$ km/h, $\rho_{max} = 450$ car/km and $v_{max} = 120$ km/h. We obtain, for the others parameters $\rho_a = 238.44$ car/km and $\rho_c = 99.35$ car/km.

5.4 The hybrid solution

Considering what has been highlighted up to this point, the best solution is an hybrid calibration method. First, we make a coarse calibration with the least-squares method, that provides the first set of parameters. Afterwards, we use the graphical estimation in order to find a more accurate value of ω_f. In fact, due to the sparseness of data in the congested phase, the value found with the last method (17 km/h) is much more reliable than the previous one and it is in accordance with values suggested in [Treiber Kesting 2013] (between 12 km/h and 20 km/h depending on the region and the highway's characteristics). Moreover, substituting the value of this parameter, only influences the right part of the function, which is the more uncertain one and leads to more lifelike values of ρ_{max}, too. Lastly, we adjust those values finding in their neighbourhood those that minimize the cost function 40.

6 Numerical results

In this chapter we present the numerical results obtained so far by means of the model described above. We report various combinations of the presented boundary conditions and input data and some tests that validate the predictive power of the model. In all simulations parameters are those chosen in Section 5.4. We don't show here any simulation that takes into account fluxes in the on- and off-ramps because their contribution to the final result is insubstantial. In addition, we avoid presenting simulations that contain the last 25 cells as the parameters estimated for those cells are not relevant, due to the fact that traffic evolution in this area is so complicated that a first-order model is not able to reproduce its behaviour in an utter way.

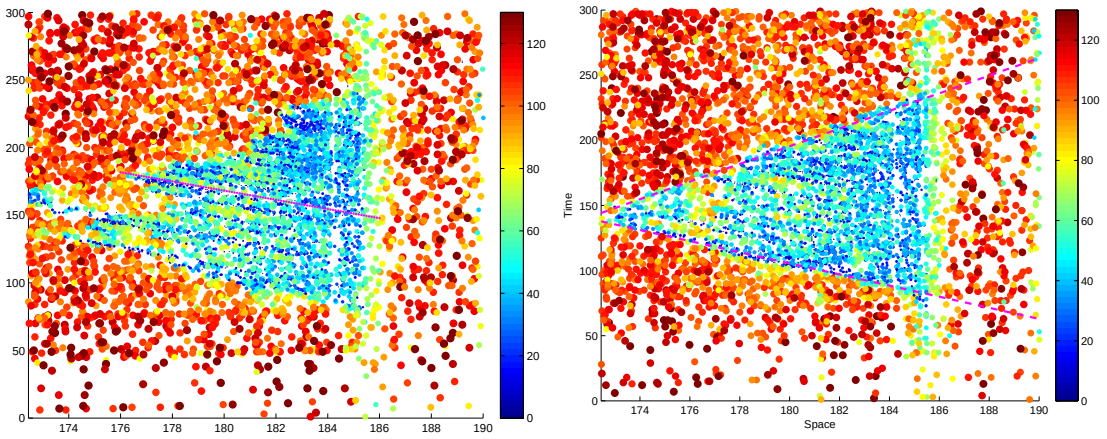

(a) ω_f. March 26$^{\text{th}}$. (b) s_1 and s_2. April 2$^{\text{nd}}$.

Figure 24: Graphical estimation

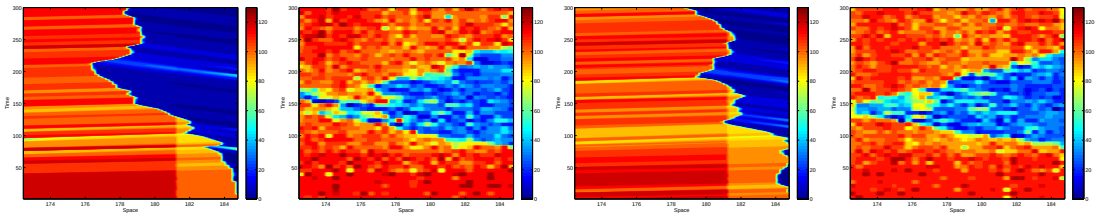

(a) March 19$^{\text{th}}$, sim. (b) March 19$^{\text{th}}$, data (c) April 2$^{\text{nd}}$, sim (d) April 2$^{\text{nd}}$, data

Figure 25: Simulation of speed field from 6 am to 11 am, cells 1 to 62, GPS flux as boundary condition.

6.1 Long term reconstructions

This section is dedicated to simulations that start at 6 am with a null initial condition and are fed with the first two boundary conditions presented in Section 3.2.1: density and flux. Simulation stops at 11 am, when no more data are available.

The first simulations we present (Fig. 25) have been done with the GPS flux as boundary condition and on the first 62 cells. The first one corresponds to day 1 (March 19$^{\text{th}}$) and the second one to day 3 (April 2$^{\text{nd}}$). We also report simulations done with loop detectors' fluxes (Fig. 26). As they're located in specific places, we only could do the computation between cell 21 and cell 64. Comparing the two, it is evident that, with the same parameters, loop detectors are much more accurate than GPS fluxes. This is due to the fact that the very small percentage of probe cars and trucks are not representative of the whole traffic situation. Lastly, we show simulations done with the second type of boundary conditions: density in ghost cells (Figures 27 and 28), that in our case are the first and the last available cells. First there are simulations done only on the first subset of cells (1 - 44), then come those made on the ensemble of the first and the second (1 - 62).

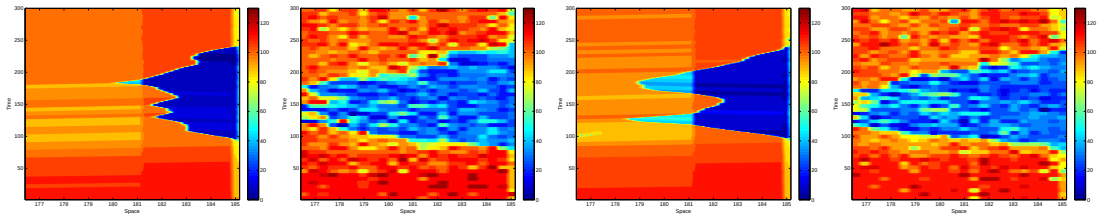

(a) March 19$^{\text{th}}$, sim. (b) March 19$^{\text{th}}$, data. (c) April 2$^{\text{nd}}$, sim. (d) April 2$^{\text{nd}}$, data.

Figure 26: Simulation of speed field from 6 am to 11 am, cells 21 to 64, loop detectors' flux as boundary condition.

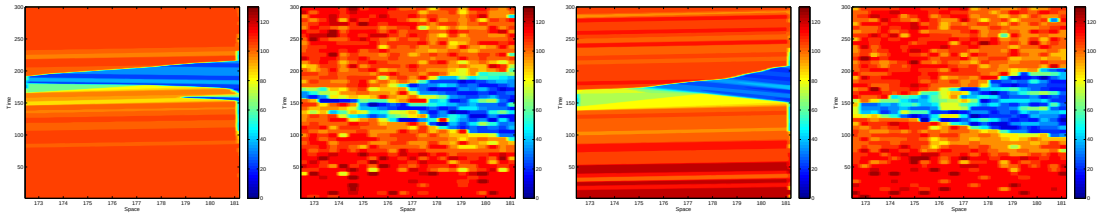

(a) March 19$^{\text{th}}$, sim. (b) March 19$^{\text{th}}$, data. (c) April 2$^{\text{nd}}$, sim. (d) April 2$^{\text{nd}}$, data.

Figure 27: Simulation of speed field from 6 am to 11 am, cells 1 to 44, density as boundary condition.

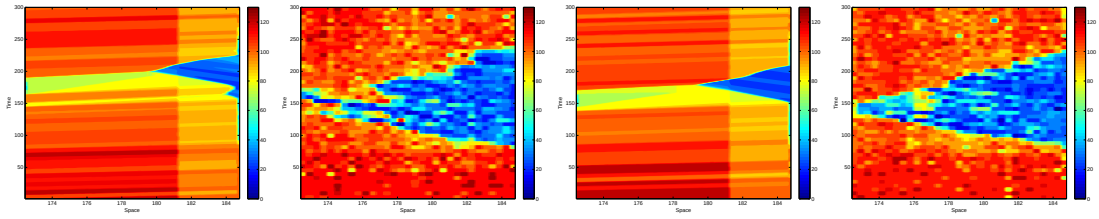

(a) March 19$^{\text{th}}$, sim. (b) March 19$^{\text{th}}$, data. (c) April 2$^{\text{nd}}$, sim. (d) April 2$^{\text{nd}}$, data.

Figure 28: Simulation of speed field from 6 am to 11 am, cells 1 to 62, density as boundary condition.

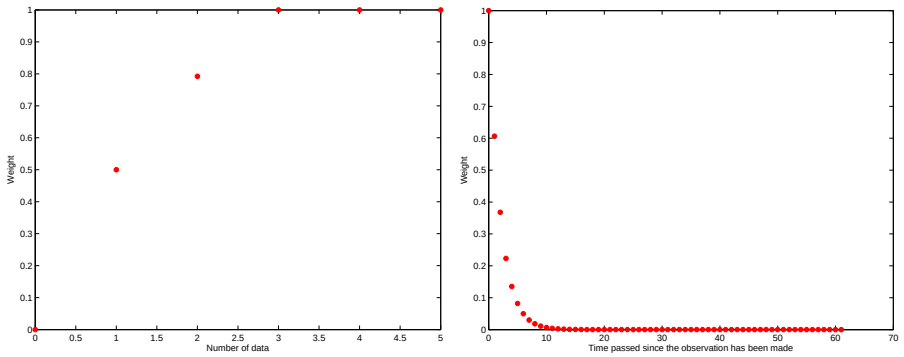

(a) Based on number of data. 1st method

(b) Based on time. 2nd method

Figure 29: Data weights

6.2 Short term forecasts

In this section, we use the third type of boundary conditions presented in Section 3.2.1. As we don't use real data to feed the simulation, we can only run it for a short time. So we choose a starting time t_0, which can be different from 6 am and then run the simulation for 30 minutes.

6.2.1 Initial condition

When we start the simulation at a time which is not 6 am, we cannot suppose that the highway is initially empty. We present here the two methods suggested in [Cristiani de Fabritiis Piccoli 2010] to estimate the initial condition from data.

First method We denote by ρ_i^n the numerical solution, by $\tilde{\rho}(x,t)$ its extension on all over the space-time box and by σ_i^n the average density in the cell (i,n) computed by means of the data and the function $\rho(v)$.

We start the simulation at time $t = 6$am with groundless pre-initial condition $\rho(x,0) \equiv 0$. Then, by means of the numerical scheme, we compute the approximate solution until time t_0, correcting it with experimental data. More precisely, once ρ_i^n is computed, we check if $\sigma_i^n(n)$ is available, i.e. there are available data the approximate solution can be corrected with. If this is the case, we set

$$\rho_i^{n,\text{corrected}} = \lambda_i^n \sigma_i^n(n) + (1-\lambda_i^n)\rho_i^n \tag{41}$$

where $\lambda_i^n \in [0,1]$ and it is chosen depending on how many data concurred to the computation of the average value $\sigma_i^n(n)$ (the more the data the more reliable the value). In particular, we chose $\lambda_i^n = \min(\log_4(d_i^n+1),1)$, where d_i^n is the number of data available at minute n in cell i. Weight values are shown in Fig. 29a.

In this fitting stage, the solution assimilates all the available data, and becomes reliable all over the road. Then, the function $\tilde{\rho}(x,t_0)$ is used as initial condition, and no more data are used to correct the solution.

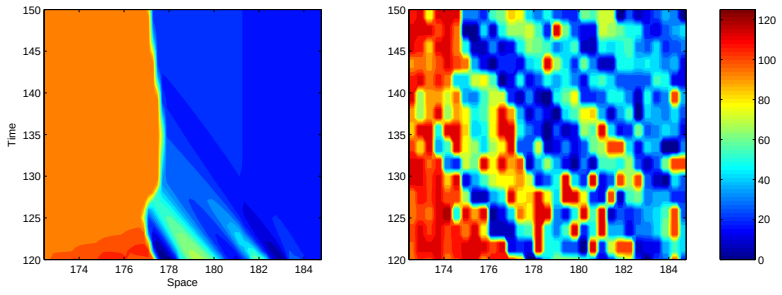

(a) 1st method

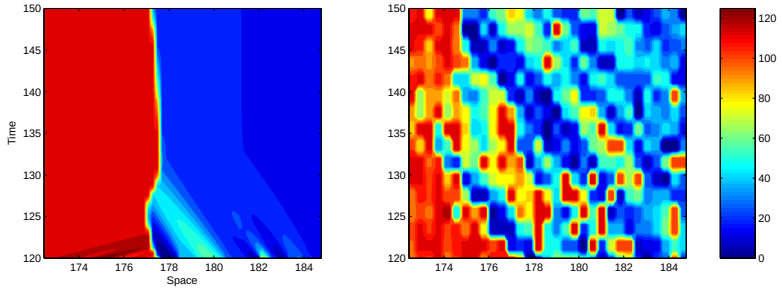

(b) 2nd method

Figure 30: 30 minute-ahead speed forecast (left) vs. actual value (right). March 19th, Antibes - Saint-Laurent-du-Var

Second method For every $i = 1, \ldots, N_x$ at time-step n corresponding to time t_0 we define

$$\rho_i^n := \frac{1}{\sum_{k=0}^{n} C_i(k,n)} \sum_{k=0}^{n} C_i(k,n)\sigma_i^k(n) \tag{42}$$

where $C_i(k,n)$ is an exponentially decreasing function of $(t_n - t_k)$ if $0 < (t_n - t_k) \leq 60$ min, and $C_i(k,n) = 0$ if $t_n - t_k > 60$ min or $\sigma_i^k(n)$ is not available. In particular, we set

$$C_i(k,n) = \begin{cases} 0 & \text{if } n-k < 0, \\ e^{\frac{(k-n)}{2}} & \text{if } 0 \leq n-k < 60, \\ 0 & \text{if } n-k \geq 60. \end{cases} \tag{43}$$

The resulting values are shown in Fig. 29b. Roughly speaking, $\phi(n)$ is a weighted average of the data measured in the hour preceding time t_n. Then we take as initial condition the extension $\tilde{\rho}(x, t_0)$ of the so computed ρ^n.

6.2.2 Congestion formation

We run the algorithm choosing $t_0 =$ 8am and the Antibes-Nice direction. We make a forecast over the following 30 minutes. Results obtained with methods 1 and 2 are shown in Fig. 30.

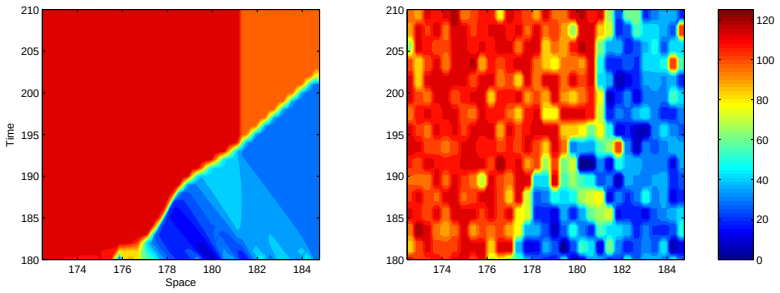

(a) 1st method

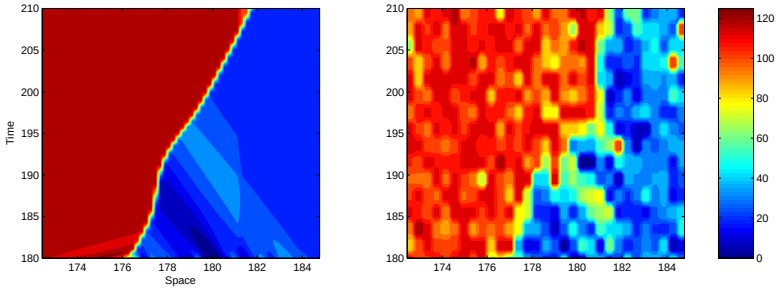

(b) 2nd method

Figure 31: 30 minute-ahead speed forecast (left) vs. actual value (right). March 19th, Antibes - Saint-Laurent-du-Var

6.2.3 Congestion extinction

We run the algorithm choosing $t_0 = 9$am and the Antibes-Nice direction. We make a forecast over the following 30 minutes. Results obtained with methods 1 and 2 are shown in Fig. 31.

6.2.4 Distribution of errors

In order to have a global idea of the abilities of the model, we compute the error distribution for several forecasts. In more detail, we run simulations with $t_0^p = 60 + 5p$ minutes, $p = 1, \dots, 36$, and $\Delta t = 10q$ minutes, $q = 1, \dots, 5$. Denoting by n_0^p the time steps corresponding to t_o^p and by Δn^q the number of time steps corresponding to $\Delta t^q, q = 1, \dots, 5$, we define an error variable $E_i^{p,q}$ at every space node $i = 1, \dots, N_x$

$$E_i^{p,q} = \frac{1}{v(\rho_i^{n_0^p + \Delta n^q})} - \frac{1}{v(\sigma_i^{n_0^p + \Delta n^q})}. \tag{44}$$

$E_i^{p,q}$ is the error made in approximating the time needed to cover 1 km at the velocity computed at node i at the end of the simulation. This error measurement is probably more meaningful than the absolute or relative error over the velocity because it is the information that drivers are interested in. In Fig. 32 we show the distribution of the errors for the chosen Δt^q. The distribution has a classical Gaussian behaviour, concentrated around zero. As Δt becomes higher, the graph becomes less symmetric, but always with a pick in zero.

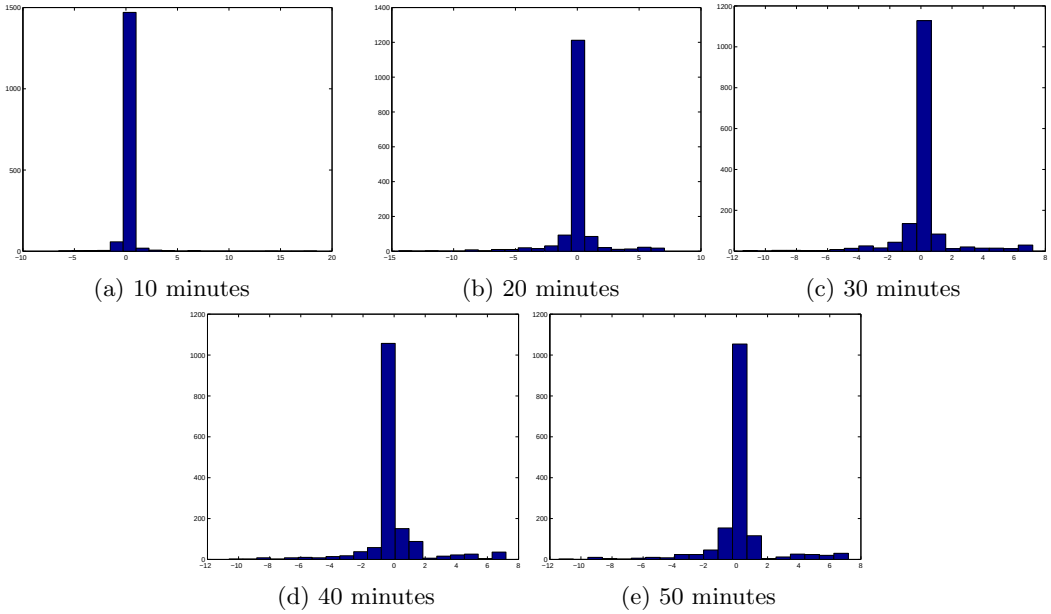

(a) 10 minutes (b) 20 minutes (c) 30 minutes

(d) 40 minutes (e) 50 minutes

Figure 32: Distribution of forecast errors

6.2.5 Travelling times

Once a forecast of the traffic condition is available, an estimate of the travelling time can be made. Thanks to the *app* developed by Eneina Gjata, Myriana Rifai and Salim Afra, interns at INRIA's OASIS team, a driver can ask for the time he/she will need to reach some destination, departing at a specified time in the future and receive an answer in a few seconds by means of the numerical scheme and parameters previously explained (for further details, see [Afra Gjata Rifai 2013]). This is made on a sophisticated platform, named PLAY, designed by the EU funded STREP project PLAY (see news.play-project.eu), where users will be able to receive and share information about traffic in real time.

To this end, it is important to notice that even if we can rely on an accurate forecast of the average velocity, this is not enough to get an accurate estimate of the travelling time. Let us assume for example that a driver has to cover 10 km. If the estimated average velocity is 60 km/h, the estimate travel time is 10 min. On the other hand, if the real velocity is 20 km/h for the first half of the road and 100 km/h for the second half (60 km/h in average), the travel time is 18 min. It is clear how important it is to compute velocity on a space grid which is as fine as possible.

In order to test the reliability of the travelling times given by the numerical simulation, we deduce from data the real travelling time between km 172.44 and 180 and compare it this value to the numerical ones. We chose to follow two cars, that we will denote by A and B respectively. Car A departed from Antibes (km 172.44) on April 2$^{\text{nd}}$ at 6.28 am and reached Cagnes-sur-Mer (km 181.2) 5 minutes later. Car B departed from the same point, the same day at 8.16 am, and the journey took 12 minutes. The tracking of the two cars are shown in Fig. 33 and 34. We computed the initial condition for numerical simulation by means of the first method, supposing that user asks for the estimate 5 minutes before entering the highway. Values are reported in table 6.

As expected, results are more reliable during the non congested phase. In fact, it is clear

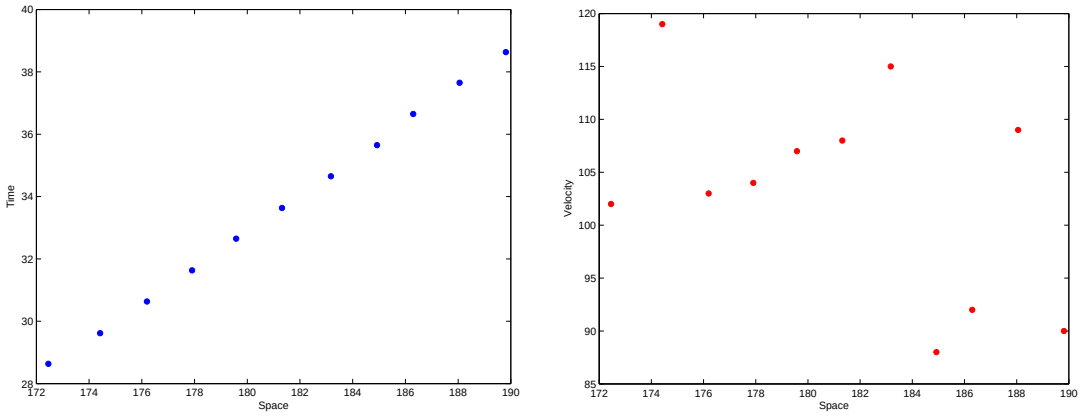

(a) Trajectory (b) Speed

Figure 33: Tracking of car A

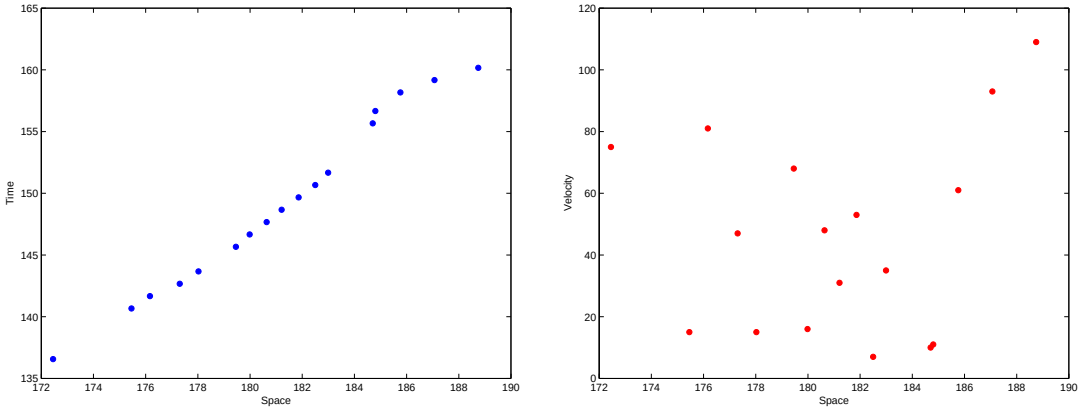

(a) Trajectory (b) Speed

Figure 34: Tracking of car B

Leaving at	Real value (min)	Estimated value (min)
6.28 am	5.0	4.9
8.16 am	12.1	14.4

Table 6: Comparison between real values and estimate values of travelling time.

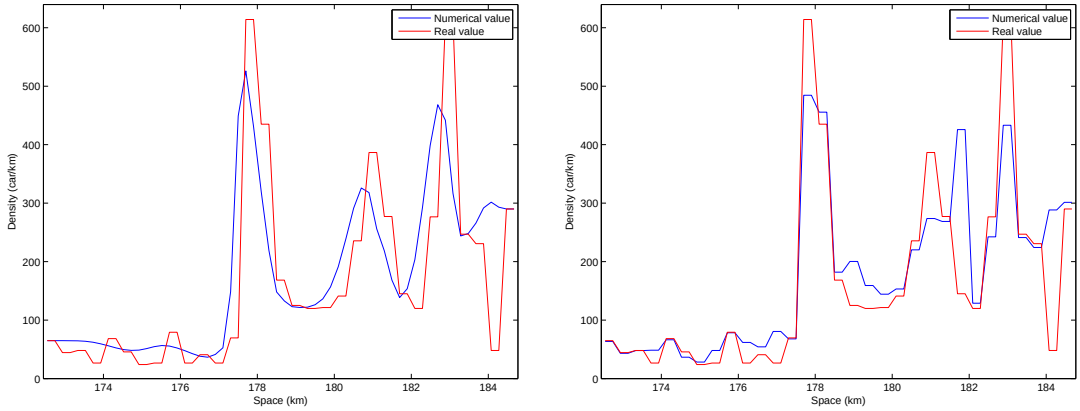

Figure 35: Initial conditions computed with methods 1(left) and 2(right).

t_0	Section	March 19$^{\text{th}}$	March 26$^{\text{th}}$	April 2$^{\text{nd}}$	April 9$^{\text{th}}$
8 am	Antibes - Cagnes-sur-Mer	43 %	41%	54 %	59 %
9 am	Antibes - Cagnes-sur-Mer	13 %	12 %	25 %	17 %
8 am	Antibes - St-Laurent-du-Var	41 %	47%	45 %	44 %
9 am	Antibes - St-Laurent-du-Var	19 %	11 %	22 %	21 %

Table 7: 1$^{\text{st}}$ Method

t_0	Section	March 19$^{\text{th}}$	March 26$^{\text{th}}$	April 2$^{\text{nd}}$	April 9$^{\text{th}}$
8 am	Antibes - Cagnes-sur-Mer	39 %	41%	51 %	49 %
9 am	Antibes - Cagnes-sur-Mer	20 %	12 %	25 %	22 %
8 am	Antibes - St-Laurent-du-Var	40 %	42%	45 %	38 %
9 am	Antibes - St-Laurent-du-Var	25 %	18 %	20 %	21 %

Table 8: 2$^{\text{nd}}$ Method

from Fig. 30 and 31 that the numerical scheme is not able to reproduce all the small local speed variations that we observe in real data.

6.2.6 Comparison between the two methods

Initial condition In Fig. 35 we show the initial conditions computed for March 26$^{\text{th}}$ at 8 am with the first and the second methods.

Relative errors We compare here the relative errors of the two methods, defined as

$$L^1(u) = \frac{\sum_j |u_{sim}(t_0 + \Delta t, j\Delta x) - u_{data}(t_0 + \Delta t, j\Delta x)|}{\sum_j |u_{data}(t_0 + \Delta t, j\Delta x)|} \tag{45}$$

where $\Delta t = 15$ min, $u_{data}(t_0 + \Delta t, j\Delta x)$ is the average density computed from data and $u_{sim}(t_0 + \Delta t, j\Delta x)$ the average on the same grid of the numerical value of density. We obtain values reported in tables 7 and 8.

Relative errors are very high when the estimated situation is congested. In fact, macroscopic models are not able to describe the stop-and-go waves, always present in congested situations (see

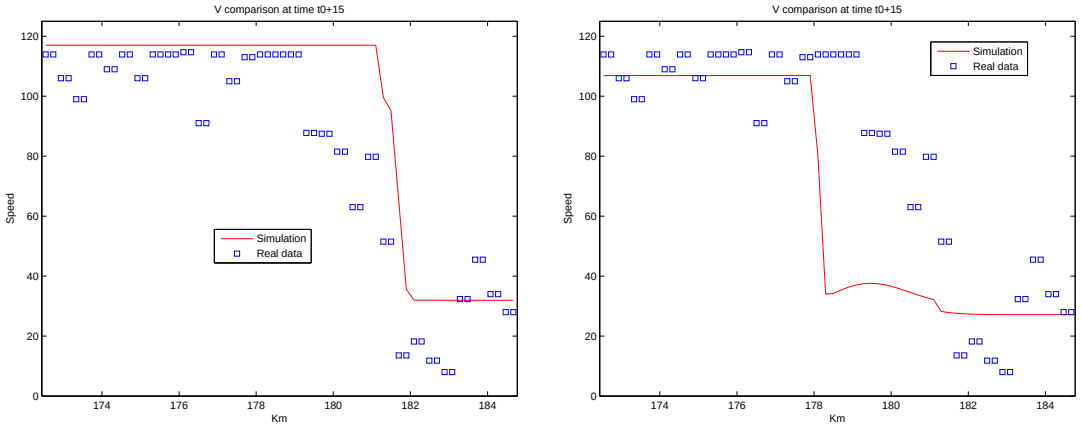

(a) Method 1 (b) Method 2

Figure 36: Congestion extinction, approximate real density and simulation at simulation result at $t_0 + 15$ min.

for example Fig. 8, stop-and-go waves are the blue lines in the light-blue zones). This happens because they only focus on integrated quantities such as the travel time, the aggregated number of vehicles, or the propagation of the congested fronts. In essence, a first order model like LWR, reproduces only the *kinematics* aspects of traffic evolution, and it is not sensitive to *dynamic* parameters determining accelerations. This allows to have a global idea of traffic evolution in time and to make good predictions, without increasing the number of parameters of the model.

On the contrary, for the non congested situations, we find values around 20%. All calibration studies in traffic estimation literature show consistently that there is a residual error of the order of 20% that not even the best model can beat. While it is not completely understood, it is known that two factors that surely play a role in this phenomenon are the choice of inappropriate fitting functions and the omitting of intra- and inter-driver variations (augmenting the model does not necessarily help since this increases the number of parameters and possibly worsens its predictive power).

Density at $t_0 + \Delta t$ We can conclude that the two methods are equivalent but the second one is more adapted to simulations that take into account the delay between the time at which data are registered and sent and time at which they are effectively received and used in the simulation.

7 Conclusions and future work

Results presented in the previous section show that, while predicting traffic evolution during all the morning is really challenging, short term predictions can be easily made. Difficulties in calibrating the model raised not only because of the complication of the concerned highway section, but they are also due to the fact that data used for the calibration came from an exiguous percentage of the total number of vehicles, which are not always representative of the *average* vehicle-driver unit. Moreover, using the LWR mathematical model, we assumed that local speed and flow are statically coupled to the density by the fundamental relation. This assumption implies instantaneous adaptation to new circumstances and leads to unbounded accelerations and other unrealistic consequences.

There are several lines of study arising from this work which could be pursued. For example, it would be interesting to test the same kind of data on some second order models. These models take into account the fact that local speed possesses its own dynamical acceleration equation, describing speed changes as a function of density, local speed, their gradients and possibly other exogenous factors. Thanks to this, they are able to describe traffic-flow instabilities leading to traffic waves and scattered flow-density data.

In addition, some aspects of this study may be improved: first, the spatio-temporal interpolation of raw data, that we used in order to have an approximated representation of the real traffic state in space and time. A recently published book by M. Treiber and A. Kesting reports an accurate way of doing the interpolation without producing artefacts such as wrong propagation velocities or even wrong propagation of congestion waves when reconstructing the continuous function of local speed average from raw data. Secondly, a deeper study of the most suitable calibration method should be done. Probably, a Monte Carlo approach or a genetic algorithm would be more effective in order to optimize parameters, see for example [Tossavainen Work 2012]. Finally, in view of applications such as the one developed by the OASIS interns, a more complete model capable of gradually incorporate data when they are available, adjusting the traffic forecast accordingly, should be implemented.

8 Acknowledgements

This research was supported by Autoroutes Trafic and the KIC EIT ICT Labs Activity no. 13052 *Multimodal Mobility.*

References

[Afra Gjata Rifai 2013] Salim Afra, Eneina Gjata, Myriana Rifai
Internship report
INRIA Research Report. September 2013

[Bardos Le Roux Nédélec 1979] C. Bardos, A. Y. Le Roux, J.C. Nédélec
First order quasilinear equations with boundary conditions
Communications in Partial Differential Equations. Published 1979

[Blandin et al. 2013] Sébastien Blandin, Juan Argote, Alexandre M. Bayen, Daniel B. Work
Phase transition model of non-stationary traffic flow: Definition, properties and solution method
ELSEVIER Transportation Research Part B. Published 15/02/2013

[Cristiani de Fabritiis Piccoli 2010] Emiliano Cristiani, Corrado de Fabritiis, Benedetto Piccoli
A Fluid Dynamic Approach for Traffic Forecast from Mobile Sensor Data
Communications in Applied and Industrial Mathematics. Published 21/06/2010

[Godunov 1959] Sergei K. Godunov
A finite difference method for the numerical computation of discontinuous solutions of the equations of fluid dynamics
Sbornik: Mathematics. Published 1959

[Herrera Work et al. 2009] Juan C. Herrera, Daniel B. Work, Ryan Herring, Xuegang Jeff Ban, Alexandre M. Bayen
Evaluation of Traffic Data Obtained via GPS-Enabled Mobile Phones: the Mobile Century

Field Experiment
UC Berkeley Center for Future Urban Transport. Published 08/01/2009

[Lebacque 1996] Jean-Patrick Lebacque
The godunov scheme and what it means for first order traffic flow models
International symposium on transportation and traffic theory N.13, Lyon, France. 24/07/1996

[Piccoli Garavello 2006] Benedetto Piccoli, Mauro Garavello
Traffic Flow on Networks
American Institute of Mathematical Sciences. March 2006

[Tossavainen Work 2012] Olli-Pekka Tossavainen, Daniel B. Work
Markov chain Monte Carlo based inverse modelling of traffic flows using GPS data
Networks and Heterogeneous Media. May 2013

[Treiber Kesting 2013] Martin Treiber, Arne Kesting
Traffic flow dynamics. Data, models and simulation.
Springer. 2013.

[Wiens Stockie Williams 2013] Jeffrey K. Wiens, John M. Stockie, JF Williams
Riemann solver for a kinematic wave traffic model with discontinuous flux
Journal of Computational Physics. February 2013

[Work et al. 2010] Daniel B. Work, Sébastien Blandin, Olli-Pekka Tossavainen, Benedetto Piccoli, Alexandre M. Bayen
A traffic model for velocity data assimilation
Oxford University Press. Published 18/01/2010

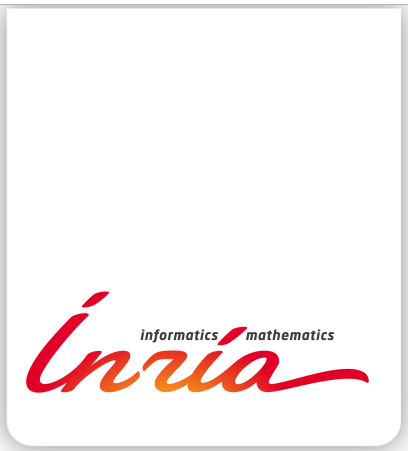

RESEARCH CENTRE
SOPHIA ANTIPOLIS – MÉDITERRANÉE

2004 route des Lucioles - BP 93
06902 Sophia Antipolis Cedex

Publisher
Inria
Domaine de Voluceau - Rocquencourt
BP 105 - 78153 Le Chesnay Cedex
inria.fr

ISSN 0249-6399